Numerical simulations of stellar collapse in scalar-tensor theories of gravity

2016 Class. Quantum Grav. 33 135002

(http://iopscience.iop.org/0264-9381/33/13/135002)

OPEN ACCESS
IOP Publishing
Classical and Quantum Gravity
Class. Quantum Grav. **33** (2016) 135002 (35pp)
doi:10.1088/0264-9381/33/13/135002

Numerical simulations of stellar collapse in scalar-tensor theories of gravity

Davide Gerosa[1], **Ulrich Sperhake**[1,2,3] **and Christian D Ott**[2,4]

[1] Department of Applied Mathematics and Theoretical Physics, Centre for Mathematical Sciences, University of Cambridge, Wilberforce Road, Cambridge CB3 0WA, UK
[2] TAPIR, Walter Burke Institute for Theoretical Physics, California Institute of Technology, Pasadena, CA 91125, USA
[3] Department of Physics and Astronomy, The University of Mississippi, University, MS 38677-1848, USA
[4] Yukawa Institute for Theoretical Physics, Kyoto University, Kyoto, Japan

E-mail: d.gerosa@damtp.cam.ac.uk

Received 23 February 2016, revised 21 April 2016
Accepted for publication 28 April 2016
Published 31 May 2016

Abstract

We present numerical-relativity simulations of spherically symmetric core collapse and compact-object formation in scalar-tensor theories of gravity. The additional scalar degree of freedom introduces a propagating monopole gravitational-wave mode. Detection of monopole scalar waves with current and future gravitational-wave experiments may constitute smoking gun evidence for strong-field modifications of general relativity. We collapse both polytropic and more realistic pre-supernova profiles using a high-resolution shock-capturing scheme and an approximate prescription for the nuclear equation of state. The most promising sources of scalar radiation are proto-neutron stars collapsing to black holes. In case of a galactic core collapse event forming a black hole, Advanced LIGO may be able to place independent constraints on the parameters of the theory at a level comparable to current solar-system and binary-pulsar measurements. In the region of the parameter space admitting spontaneously scalarised stars, transition to configurations with prominent scalar hair before black-hole formation further enhances the emitted signal. Although a more realistic treatment of the microphysics is necessary to fully investigate the occurrence of spontaneous scalarisation of neutron star remnants, we speculate that formation of such objects could

constrain the parameters of the theory beyond the current bounds obtained with solar-system and binary-pulsar experiments.

Keywords: modified theories of gravity, gravitational waves, supernovae

(Some figures may appear in colour only in the online journal)

1. Introduction

General relativity (GR) is currently assumed to be the standard theory of gravity, and has so far passed all experimental tests with flying colours [1–4]. Theoretical and observational evidence, however, suggests that some modifications of GR may be inevitable. Cosmological and astrophysical observations require most of the energy content of the Universe to be present in the form of dark energy and dark matter [5–7]. On theoretical grounds, GR is expected to represent the low-energy limit of a more fundamental (quantum) theory [8]. Presently considered candidates for such theories predict modifications of GR at higher energies which also provide means to circumvent the formation of mathematical singularities inevitable in GR [9].

Attempts to generalise GR in these directions often involve additional fields that mediate the gravitational interaction together with the spacetime metric. The simplest class of such models is that of scalar-tensor (ST) theories, where one scalar field is included in the gravitational sector of the action. Ever since the pioneering work of Jordan, Fierz, Brans, and Dicke [10–12], ST theories have received a great deal of attention, both from a theoretical and a phenomenological point of view (see e.g. [13–17] and references therein). This class of theories is *simple enough* to allow for detailed predictions to be worked out, but also *complicated enough* to introduce a richer phenomenology leading to potentially observable deviations from GR. ST theories make predictions in the largely untested strong-field regime, while remaining compatible with the weak-field constraints imposed on GR by solar system experiments (see section 3.2 below).

Black hole (BH) spacetimes might at first glance appear to represent an ideal testing ground for strong-field effects. The classical no-hair theorems, first proven for Brans–Dicke theory [18–20] and later extended to a wider range of ST theories (see [21, 22] for reviews), however, strongly constrain the potential for deviations of BH spacetimes in ST theory from their GR counterparts. At leading post-Newtonian (PN) order, for example, the dynamics of a BH binary in Brans–Dicke theory is indistinguishable from the GR case [23]. Indeed, considering the ST field equations given below as equations (2.5)–(2.8), one immediately sees that vacuum solutions of GR are also solutions to the ST equations with a constant scalar field. Non-trivial BH dynamics can still be obtained by relaxing some of the fundamental ingredients of the no-hair theorems as for example a non-vanishing potential term [24] or non-asymptotic flatness [25]. Due to the additional coupling introduced by the energy momentum tensor in the ST equations, however, compact matter sources such as neutron stars (NSs) and collapsing protoneutron stars forming BHs appear to be more promising objects for exploring observational signatures of ST theories.

Guided by this expectation, we shall focus in this paper on the formation of compact objects through gravitational collapse. Gravitational collapse is the expected evolutionary endpoint of stars of zero-age main sequence (ZAMS) mass of $10M_{\odot} \lesssim M \lesssim 130M_{\odot}$ [26–28]. After exhausting their available fuel, the star's central core (mostly made of iron group nuclei) collapses under the strength of gravity as it exceeds its effective Chandrasekhar mass [29].

Collapse proceeds until mass densities become comparable to those of nuclear matter. Thereafter, the increasingly repulsive character of the nuclear interactions leads to core bounce, which results in an outgoing hydrodynamic shock. The outgoing shock soon stalls because of dissociation of nuclei and neutrino emission in the post-shock region, and must be revived to successfully drive a supernova (SN) explosion [29]. The physical mechanism responsible for the shock revival is still a topic of active research (see e.g. [30] and references therein). Multi-dimensional fluid instabilities and neutrino interactions are generally believed to play a crucial role in driving most SN explosions with the possible exception of hyper-energetic ones [31, 32]. One single core-collapse SN provides photon luminosities comparable to those of an entire Galaxy and outshines all stars in the Universe in neutrinos. If the explosion is successful, a NS is left behind. If the explosion fails or is very weak, continued accretion will push the central NS over its maximum mass of $2-3M_{\odot}$ and lead to the formation of a BH. The details of BH formation depend on the structure of the progenitor star and on the nuclear equation of state (EOS) [26].

ST theories may play a crucial role in this picture of NS and BH formation. A peculiar nonlinear effect called 'spontaneous scalarisation' [33, 34]—somewhat similar to spontaneous magnetisation in ferromagnets—represents a particularly strong form of non-trivial scalar-field dynamics leading to additional branches of stationary NS families (see also [35–37] for dynamical scalarisation in binary NS systems). Moreover, ST theories provide a new channel for emission of gravitational waves (GWs) in stellar collapse. Whereas in GR conservation of mass and momentum exclude monopole and dipole radiation, monopole waves are permitted in ST theories in the form of scalar radiation, the so-called *breathing mode*. Detection of this breathing mode generated by a galactic SN would constitute smoking-gun evidence for a deviation from GR in the strong-field regime. Such tests of GR represent a major scientific goal [2] of the new era of GW astronomy initiated with the recent breakthrough detection of GW150914 [38], and thus add to the enormous scientific potential of exploring the physics of stellar collapse with GWs (see [39] for a comprehensive review on the topic).

The impact of ST theories on the equilibrium structure of NSs has been extensively studied in the literature (see, e.g., [33, 40–44]). Surprisingly few studies, however, have been devoted to their formation processes. Following pioneering numerical relativity simulations in Brans–Dicke theory [45], early studies have been devoted to dust-fluid collapse [46–49]. The collapse of NSs into BHs [50] and the transition between different static NS branches [51] was first addressed by Novak using pseudo-spectral methods. To the best of our knowledge, the only published simulations of NS formation in ST theories have been presented by Novak and Ibáñez in [52], who combined pseudo-spectral techniques and high-resolution shock-capturing to study core collapse. The only other study we are aware of is [53], which numerically models the collapse of spherically symmetric fluids with a Γ-law EOS in Brans–Dicke theory and finds the monopole radiation to dominate at frequencies near the GW detectors' maximum sensitivity regime $f\sim 100$ Hz, independently of the Brans–Dicke coupling parameter. The systematic exploration of GW emission from core collapse in ST theories thus represents a largely uncharted area in SN research. The dawning age of observational GW physics makes the filling of this gap a timely task, the first step of which is the main goal of this paper.

For this purpose, we have extended the open-source code GR1D of O'Connor and Ott [54] to ST theory and performed numerical simulations of NS and BH formation following core collapse to address the detectability of the monopole GWs with Advanced LIGO [55, 56] and the proposed Einstein telescope [57]. We tackle the following questions.

- Are non-trivial scalar-field profiles and correspondingly large amplitudes in the scalar radiation naturally triggered in compact remnants following stellar collapse?
- Can future GW observations of core collapse provide smoking gun evidence for deviations from GR in the framework of ST theories?

This paper is organised as follows. The action and the evolution equations of the theory are presented in section 2. Additional physical ingredients entering our simulations are given in section 3. Our numerical procedure is described in section 4. We present our results on core collapse dynamics and monopole GW emission in section 5. We summarise our findings in section 6. Supporting material is provided online at [58]. Throughout the paper, we generally use geometrical units $c = G = 1$, but occasionally restore factors of G for clarity of presentation.

2. Evolution equations

In this section, we first review different ways to formulate ST theories and then arrive at the equations for the metric, scalar field, and matter sector in general covariant form (section 2.1). Next, we derive the hydrodynamic equations for the matter sources, the metric and scalar field for the specific case of radial-gauge, polar-slicing coordinates (section 2.2).

2.1. A tale of two formulations

In ST theories, gravity is mediated by the spacetime metric $g_{\mu\nu}$ and an additional scalar field ϕ. The most general action which (i) involves a single scalar field coupled non-minimally to the metric, (ii) is invariant under space–time diffeomorphisms, (iii) is at most quadratic in derivatives of the field, and (iv) satisfies the weak equivalence principle can be written in the form [1, 13, 59]

$$S = \int \mathrm{d}x^4 \sqrt{-g}\left[\frac{F(\phi)}{16\pi G}R - \frac{1}{2}g^{\mu\nu}(\partial_\mu\phi)(\partial_\nu\phi) - V(\phi)\right] + S_m(\psi_m, g_{\mu\nu}). \tag{2.1}$$

Here, d^4x is the standard coordinate volume element, R is the Ricci scalar built from $g_{\mu\nu}$, $g = \det g_{\mu\nu}$ and the symbol ψ_m collectively denotes all non-gravitational fields. The theory has only two free functions of the scalar field: the potential $V = V(\phi)$ and the coupling function[5] $F = F(\phi)$. If the potential V is a slowly varying function of ϕ—as expected on cosmological grounds, see [60]—it causes negligible effects on the propagation of ϕ on stellar scales. For simplicity, we thus set $V = 0$ throughout this paper; GR is then recovered for $F = 1$. Details on the choice of the coupling function F are postponed to section 3.2.

The weak equivalence principle—which has been verified experimentally to very high precision [3]—is guaranteed to hold as long as the matter part of the action S_m does not couple to the scalar field, and its motion is therefore governed by the geodesics of the metric $g_{\mu\nu}$. In this formulation, the scalar field does not interact with ordinary matter directly, but influences the motion of particles exclusively through its coupling with the spacetime metric.

The theory described by the action (2.1) is said to be formulated in the *Jordan frame* [10]. Probably the most famous case of a ST theory, though by now severely constrained by solar-system tests [61], is Brans–Dicke theory [12]: the specific theory obtained by setting $F(\phi) = 2\pi\phi^2/\omega_{\rm BD}$ where $\omega_{\rm BD}$ is constant [59].

[5] Another common notation for the coupling function is $A = F^{-1/2}$ (see, e.g., [13, 33, 34]).

Alternatively to the above Jordan-frame description, ST theories can also be formulated in the so-called *Einstein frame*. Here, one considers the conformal transformation

$$\bar{g}_{\mu\nu} = F g_{\mu\nu}, \tag{2.2}$$

and the action of equation (2.1) becomes

$$S = \frac{1}{16\pi G}\int \mathrm{d}x^4 \sqrt{-\bar{g}}\,[\bar{R} - 2\bar{g}^{\mu\nu}(\partial_\mu\varphi)(\partial_\nu\varphi)] + S_m[\psi_m, \bar{g}_{\mu\nu}/F]. \tag{2.3}$$

The Ricci scalar $\bar{R}$ is now built from the Einstein metric $\bar{g}_{\mu\nu}$ and φ is a redefinition of the scalar field ϕ through [59, 62],

$$\frac{\partial\varphi}{\partial\phi} = \sqrt{\frac{3}{4}\frac{F_{,\phi}{}^2}{F^2} + \frac{4\pi G}{F}}. \tag{2.4}$$

The key advantage resulting from this conformal transformation is a minimal coupling between the conformal metric and the scalar field, evident at the level of the action. The fact that such a redefinition of the theory exists has an important consequence for attempts to constrain the theory's parameters through observations of compact objects: BHs are less suitable to obtain such constraints because the action (2.3) in vacuum ($S_m = 0$) reduces to the Einstein–Hilbert action of GR with a minimally coupled scalar field. In the action as well as the field equations given further below, it is evident that matter sources represent an additional and more straightforward channel to couple the metric and scalar sectors.

The equations of motion in the Jordan frame can be obtained by varying the action (2.1) with respect to the spacetime metric $g_{\mu\nu}$ and the scalar field ϕ:

$$G_{\mu\nu} = \frac{8\pi}{F}(T^F_{\mu\nu} + T^\phi_{\mu\nu} + T_{\mu\nu}), \tag{2.5}$$

$$T^F_{\mu\nu} = \frac{1}{8\pi}(\nabla_\mu\nabla_\nu F - g_{\mu\nu}\nabla^\rho\nabla_\rho F), \tag{2.6}$$

$$T^\phi_{\mu\nu} = \partial_\mu\phi\partial_\nu\phi - \frac{1}{2}g_{\mu\nu}\partial^\nu\phi\partial_\nu\phi, \tag{2.7}$$

$$\nabla^\rho\nabla_\rho\phi = -\frac{1}{16\pi}F_{,\phi}R. \tag{2.8}$$

Combining the Bianchi identities with the field equations can be shown to imply that the matter part of the energy momentum tensor

$$T_{\mu\nu} = \frac{2}{\sqrt{-g}}\frac{\delta S_m}{\delta g_{\mu\nu}}, \tag{2.9}$$

is conserved on its own, i.e.

$$\nabla_\mu T^{\mu\nu} = 0. \tag{2.10}$$

This feature makes the Jordan frame particularly suitable for studying stellar collapse: the matter equations, which are expected to develop shocks, do not need to be modified from their GR counterparts (see section 2.2.3). The drawback of this choice is that the scalar field is not minimally coupled to the metric, i.e. the Hilbert term in the action (2.1) acquires a ϕ-dependent factor. This factor $F(\phi)$ leads to the term $T^F_{\mu\nu}$ on the right-hand side of equation (2.5) additionally to the minimally coupling term $T^\phi_{\mu\nu}$ and the standard matter sources $T_{\mu\nu}$.

2.2. Equation of motions

We now restrict the equations of motion to spherical symmetry in radial-gauge, polar-slicing coordinates [63]. The line element in the Jordan frame is

$$\mathrm{d}s^2 = g_{\mu\nu}\mathrm{d}x^\mu \mathrm{d}x^\nu = -\alpha^2 \mathrm{d}t^2 + X^2 \mathrm{d}r^2 + \frac{r^2}{F} d\Omega^2, \tag{2.11}$$

where the metric functions $\alpha = \alpha(t, r)$ and $X = X(t, r)$ can be more conveniently rewritten in terms of the metric potential

$$\Phi = \ln(\sqrt{F}\alpha), \tag{2.12}$$

and the enclosed mass

$$m = \frac{r}{2}\left(1 - \frac{1}{FX^2}\right). \tag{2.13}$$

Note that in equation (2.11) we multiplied the angular part of the metric $\mathrm{d}\Omega^2$ by a factor $1/F$, thus effectively imposing the radial gauge in the Einstein frame. In this formulation, the (Jordan-frame) areal radius is given by $r/\sqrt{F}$. This choice allows for comparisons with [50–52], where the analysis is entirely carried out in the Einstein frame. Likewise, Φ and m are Einstein-frame variables and their definition in terms of the Jordan metric components in equations (2.12) and (2.13) acquires factors of F.

Following [54], we assume ideal hydrodynamics as described by an energy–momentum tensor of the form

$$T_{\alpha\beta} = \rho h u_\alpha u_\beta + P g_{\alpha\beta}, \tag{2.14}$$

and the matter current density

$$J^\alpha = \rho u^\alpha. \tag{2.15}$$

Here ρ is the baryonic density, P is the fluid pressure, h is the specific enthalpy (which is related to the specific internal energy ϵ and the pressure P by $h = 1 + \epsilon + P/\rho$), and u^μ is the four-velocity of the fluid. Spherical symmetry implies

$$u^\mu = \frac{1}{\sqrt{1 - v^2}}\left[\frac{1}{\alpha}, \frac{v}{X}, 0, 0\right], \tag{2.16}$$

where $v = v(t, r)$.

The equations of motion can be reformulated in flux conservative form using *conserved* variables and thus become amenable to a numerical treatment using high-resolution shock-capturing schemes [64, 65]. These conserved variables D, S^r and τ are related to the to the *primitive* variables ρ, ϵ, v and P by

$$D = \frac{\rho X}{F\sqrt{F}\sqrt{1 - v^2}}, \tag{2.17}$$

$$S^r = \frac{\rho h v}{F^2(1 - v^2)}, \tag{2.18}$$

$$\tau = \frac{\rho h}{F^2(1 - v^2)} - \frac{P}{F^2} - D. \tag{2.19}$$

The definitions above generalise equation (8) in [54] to ST theory. We take advantage of the Einstein-frame scalar-field redefinition $\phi \to \varphi$ of equation (2.4) because it simplifies the wave equation (2.8). Moreover, the space of ST theories and the weak-field experimental

constraints are traditionally described in terms of φ (see section 3.2). Following [50–52], we introduce auxiliary variables for the derivatives of the scalar field defined by

$$\eta = \frac{\partial_r \varphi}{X}, \qquad \psi = \frac{\partial_t \varphi}{\alpha}. \tag{2.20}$$

2.2.1. Metric equations. The evolution equations (2.5)–(2.7) for the metric potential Φ and the mass function m expressed in terms of the conserved variables read

$$\partial_r \Phi = X^2 F\left[\frac{m}{r^2} + 4\pi r\left(S^r v + \frac{P}{F^2}\right) + \frac{r}{2F}(\eta^2 + \psi^2)\right], \tag{2.21}$$

$$\partial_r m = 4\pi r^2(\tau + D) + \frac{r^2}{2F}(\eta^2 + \psi^2), \tag{2.22}$$

$$\partial_t m = r^2 \frac{\alpha}{X}\left(\frac{1}{F}\eta\psi - 4\pi S^r\right). \tag{2.23}$$

These equations are not independent; the last equation for $\partial_t m$ directly follows from the other two combined with the conservation of the energy momentum tensor (2.10). For convenience, we follow standard practice and compute the metric functions using the constraints (2.21) and (2.22) and discard the time evolution equation for m.

From equation (2.21), we further notice that the metric potential Φ is determined only up to an additive constant. In GR, this freedom is commonly used to match the outer edge of the computational domain to an external Schwarzschild metric. This cannot be done in ST theories, as such theories do not obey a direct analogue of the Birkhoff theorem [66, 67]. We therefore specify a boundary condition for Φ using the method put forward by Novak [50]: Φ is constrained on the outer boundary of the computational domain by requiring that

$$K = \frac{\mathrm{e}^{\Phi}}{\sqrt{1 - \frac{2m}{r}}} \tag{2.24}$$

is approximately constant in the weak-field regime, far away from the star. K is then evaluated for the initial profile (see section 2), fixed to be constant during the evolution and determines Φ on the outer edge of the grid $r = R_{\rm out}$ by inverting (2.24)

$$\Phi(R_{\rm out}) = \ln\left(K\sqrt{1 - \frac{2m(R_{\rm out})}{R_{\rm out}}}\right). \tag{2.25}$$

Note that the Birkhoff theorem in GR corresponds to the case $K = 1$. The error incurred from this procedure can be estimated by comparing results obtained for different extents of the computational domain. We obtain variations of order $|\Delta\varphi/\varphi| \sim 10^{-3}$ at the radius of extraction when the grid extent is decreased by a factor 2 (see section 4.1 for more details on our numerical setup). Similar errors are detected in the collapse of a ST polytrope if K is set to 1, rather than evaluated from the initial profile.

2.2.2. Scalar-field equations. The wave equation for the scalar field (2.8) can be written as a first-order system using the definitions (2.20) and the identity $\partial_t\partial_r\eta = \partial_r\partial_t\eta$ to obtain

$$\partial_t \varphi = \alpha\psi, \tag{2.26}$$

$$\partial_t \eta = \frac{1}{X}\partial_r(\alpha\psi) - rX\alpha\eta(\eta\psi - 4\pi F\ S^r) + \frac{F_{,\varphi}}{2F}\alpha\eta\psi, \tag{2.27}$$

$$\partial_t \psi = \frac{1}{r^2 X}\partial_r(\alpha r^2\eta) + rX\alpha\psi(\eta\psi - 4\pi F\ S^r) - \frac{F_{,\varphi}}{2F}\alpha\psi^2 + 2\pi\alpha\left(\tau - S^r v + D - 3\frac{P}{F^2}\right)F_{,\varphi}. \tag{2.28}$$

In order to prescribe the behaviour of φ at the outer boundary, we consider the asymptotic behaviour of the scalar field at spatial infinity [13]

$$\varphi(r) = \varphi_0 + \frac{\omega}{r} + \mathcal{O}\left(\frac{1}{r^2}\right), \tag{2.29}$$

where $\varphi_0 =$ const and and ω denotes the *scalar charge* of the star. Physically, we require that no radiation enters the spacetime from infinity and therefore impose an outgoing boundary condition [68] at spatial infinity

$$\lim_{r\to\infty}\varphi(t,\ r) = \varphi_0 + \frac{f(t-r)}{r} + \mathcal{O}(r^{-2}), \tag{2.30}$$

where f is a free function of retarded time. This condition can be translated into the following differential expressions for η and ψ,

$$\partial_t\psi + \partial_r\psi + \frac{\psi}{r} = 0, \tag{2.31}$$

$$\partial_t\eta + \partial_r\eta + \frac{\eta}{r} - \frac{\varphi - \varphi_o}{r^2} = 0, \tag{2.32}$$

and the scalar field φ is directly obtained from equation (2.26). As shown in more detail below (see equation (3.8) and the following discussion), the value of φ_0 is degenerate with one of the parameters used to describe the coupling function and is set to zero in our study without loss of generality.

In practice, our computational domain extends to large but finite radii and we approximate the physical boundary conditions by imposing equations (2.31) and (2.32) at the outer edge rather than at infinity. As already mentioned, we have tested the influence of the outer boundary location on our results and observe only tiny variations of the order of $|\Delta\varphi/\varphi| \sim 10^{-3}$ in the extraction region when comparing with simulations performed with $R_{\rm out}$ twice as large.

2.2.3. Matter equations in flux-conservative form. The evolution equations (2.5)–(2.8) can be conveniently written in flux-conservative form [65, 69],

$$\partial_t\mathbf{U} + \frac{1}{r^2}\partial_r\left[r^2\frac{\alpha}{X}\mathbf{f}(\mathbf{U})\right] = \mathbf{s}(\mathbf{U}), \tag{2.33}$$

where $\mathbf{U}$ is the vector of the conserved variables $\mathbf{U} = [D,\ S^r,\ \tau]$ defined in equations (2.17)–(2.19). The fluxes $\mathbf{f}(\mathbf{U}) = [f_D, f_{S^r}, f_\tau]$ and the source $\mathbf{s}(\mathbf{U}) = [s_D,\ s_{S^r},\ s_\tau]$ are given by

$$f_D = Dv, \tag{2.34}$$

$$f_{S^r} = S^r v + \frac{P}{F^2}, \tag{2.35}$$

$$f_\tau = S^r - Dv, \tag{2.36}$$

$$s_D = -D\frac{F_{,\varphi}}{2F}\alpha(\psi + \eta v), \tag{2.37}$$

$$\begin{aligned} s_{S^r} = {} & (S^r v - \tau - D)\alpha X F\left(8\pi r\frac{P}{F^2} + \frac{m}{r^2} - \frac{F_{,\varphi}}{2F^2 X}\eta\right) + \frac{\alpha X}{F}P\frac{m}{r^2} + 2\frac{\alpha P}{rXF^2} \\ & - 2r\alpha X S^r \eta\psi - \frac{3}{2}\alpha\frac{P}{F^2}\frac{F_{,\varphi}}{F}\eta - \frac{r}{2}\alpha X(\eta^2 + \psi^2)\left(\tau + \frac{P}{F^2} + D\right)(1 + v^2), \end{aligned} \tag{2.38}$$

$$\begin{aligned} s_\tau = {} & -\left(\tau + \frac{P}{F^2} + D\right)r\alpha X[(1 + v^2)\eta\psi + v(\eta^2 + \psi^2)] \\ & + \frac{\alpha}{2}\frac{F_{,\varphi}}{F}\left[Dv\eta + \left(S^r v - \tau + 3\frac{P}{F^2}\right)\psi\right]. \end{aligned} \tag{2.39}$$

Note that [52] misses a factor $1/a$ (in their notation) inside the argument of the radial derivative in their equation (11). Inclusion of this factor and pulling the term proportional to ηv in equation (2.37) out of the radial derivative enables us to cast the evolution equation for D in the same form (2.33) as the other matter equations. For the integration of the evolution equation for D, we therefore do not need the additional considerations described in section 2.1 of [52].

The hyperbolic structure of the system of equation (2.33) is dictated by the Jacobian matrix of the fluxes [70],

$$\mathbf{J}_\mathbf{U} = \frac{\partial \mathbf{f}(\mathbf{U})}{\partial \mathbf{U}}. \tag{2.40}$$

The characteristic speeds associated with the propagation of the matter fields are the eigenvalues λ of $\mathbf{J}_\mathbf{U}$,

$$\lambda = \left[v,\ \frac{v + c_\mathrm{s}}{1 + v\,c_\mathrm{s}},\ \frac{v - c_\mathrm{s}}{1 - v\,c_\mathrm{s}}\right]. \tag{2.41}$$

Here $c_\mathrm{s} = \sqrt{(\mathrm{d}P/\mathrm{d}\rho)_S/h}$ (S is the entropy) is the local speed of sound given for our choice of EOS of the form $P = P(\rho, \epsilon)$ by

$$h\,c_\mathrm{s}^2 = \frac{\partial P}{\partial \rho} + \frac{P}{\rho^2}\frac{\partial P}{\partial \epsilon}. \tag{2.42}$$

The characteristic speeds are therefore exactly the same as in GR, since they do not depend on the conformal factor F. The high-resolution shock-capturing scheme implemented in GR1D for GR [54] can therefore be used in ST theories as well, provided the conserved variables $\mathbf{U}$ and their fluxes $\mathbf{f}(\mathbf{U})$ are generalised using the expressions presented above.

3. Physical setup

In this section, we discuss in more detail the physical ingredients entering our simulations. We discuss the EOS for the fluid used in our work (section 3.1), the various choices for the coupling function that relate the physical metric to its conformally rescaled counterpart (section 3.2) and the initial stellar profiles used in our study (section 3.3). We also provide

information on the quantities used to compare GW signals and detector sensitivities in the context of monopole waves (section 3.4).

3.1. Equation of state

An EOS is required to close the hydrodynamical system of equations. Specifically, it provides a prescription for the pressure P and other thermodynamic quantities as a function of the mass density, internal energy (or temperature), and possibly the chemical composition. In this paper we study stellar collapse using the so-called *hybrid* EOS. This EOS was introduced in [71] and qualitatively captures in closed analytic form the expected stiffening of the nuclear matter EOS at nuclear density and includes non-isentropic (thermal) effects to model the response of shocked material. The hybrid EOS was widely used in early multi-dimensional core-collapse simulations (e.g. [72, 73]), and the results of simulations using a hybrid EOS have been compared in detail with those obtained with modern finite-temperature EOS; see e.g. [74, 75].

The hybrid EOS consists of a *cold* and a *thermal* part:

$$P = P_{\rm c} + P_{\rm th}. \tag{3.1}$$

The cold component $P_{\rm c}$ is modelled in piecewise polytropic form with adiabatic indices Γ_1 and Γ_2,

$$P_{\rm c} = \begin{cases} K_1 \rho^{\Gamma_1} & \text{if} \quad \rho \leqslant \rho_{\rm nuc}, \\ K_2 \rho^{\Gamma_2} & \text{if} \quad \rho > \rho_{\rm nuc}. \end{cases} \tag{3.2}$$

This expression models both the pressure contribution from relativistic electrons, which dominates at $\rho \leqslant \rho_{\rm nuc}$, and the stiffening at nuclear density due to the repulsive character of the nuclear force. The two components are matched at 'nuclear density' which we set to $\rho_{\rm nuc} = 2 \times 10^{14}$ g cm^{-3} following [73]. We set $K_1 = 4.9345 \times 10^{14}$ [cgs], as predicted for a relativistic degenerate gas of electrons with electron fraction $Y_{\rm e} = 0.5$ [76], while $K_2 = K_1 \rho_{\rm nuc}^{\Gamma_1 - \Gamma_2}$ is then obtained from requiring continuity in P at $\rho = \rho_{\rm nuc}$. The specific internal energy follows from the first law of thermodynamics applied to the case of adiabatic processes

$$\epsilon_{\rm c} = \begin{cases} \frac{K_1}{\Gamma_1 - 1} \rho^{\Gamma_1 - 1} & \text{if} \quad \rho \leqslant \rho_{\rm nuc}, \\ \frac{K_2}{\Gamma_2 - 1} \rho^{\Gamma_2 - 1} + E_3 & \text{if} \quad \rho > \rho_{\rm nuc}, \end{cases} \tag{3.3}$$

where the integration constant E_3 is determined by continuity at $\rho = \rho_{\rm nuc}$. The thermal contribution $P_{\rm th}$ is described by a Γ-law with adiabatic index $\Gamma_{\rm th}$,

$$P_{\rm th} = (\Gamma_{\rm th} - 1) \rho \epsilon_{\rm th}, \tag{3.4}$$

where $\epsilon_{\rm th} = \epsilon - \epsilon_{\rm c}$ is the thermal contribution to the internal energy, computed from the primitive variable ϵ. The flow is adiabatic before bounce, implying that $\epsilon \simeq \epsilon_{\rm c}$ and the total pressure is described by considering only its cold contribution. At core bounce, however, the hydrodynamic shock results in non-adiabatic flow and thus triggers the onset of a non-negligible thermal contribution to the EOS.

We consider a hybrid EOS characterised by three parameters: Γ_1, Γ_2 and $\Gamma_{\rm th}$. The physical range of these adiabatic indices has been explicitly studied in [74, 75], where $2 + 1$ GR simulations of core collapse were used to compute the effective adiabatic index of the finite-temperature EOS of Lattimer and Swesty [77, 78] and Shen *et al* [79, 80]. In the collapse phase, electron capture decreases the effective adiabatic index below the value $\Gamma_1 = 4/3$ predicted for a relativistic gas of electrons. More precisely, comparisons with more detailed

simulations yields a range from $\Gamma_1 \simeq 1.32$ to $\Gamma_1 \simeq 1.28$ [74, 75, 81]. In particular, lower values of Γ_1 are found when deleptonisation is taken into account because electron capture onto nuclei before neutrino trapping decreases Y_e for given ρ, thus softening the EOS. Collapse is stopped by the stiffening of the EOS at nuclear density which raises the effective adiabatic index Γ_2 above $4/3$. Reference [75] finds $\Gamma_2 \simeq 3.0$ for the Shen *et al* EOS and $\Gamma_2 \simeq 2.5$ for the Lattimer–Swesty EOS. Finally, the thermal adiabatic index $\Gamma_{\rm th}$ models a mixture of relativistic and non-relativistic gas, and is therefore physically bounded to $4/3 < \Gamma_{\rm th} < 5/3$. We select fiducial values $\Gamma_1 = 1.3$, $\Gamma_2 = 2.5$, $\Gamma_{\rm th} = 1.35$ for our code tests presented in section 4, and explore a more extended parameter grid around this model in section 5.

3.2. Coupling function

As introduced in section 2.1, ST theories with a single scalar field and vanishing potential are described by a single free function $F(\varphi)$. The phenomenology of ST theories is simplified, however, by the fact that all modifications of gravity at first PN order depend only on two parameters. These are the asymptotic values of the first and second derivatives of $\ln F$ [13, 14, 34] [6],

$$\alpha_0 = -\frac{1}{2}\frac{\partial \ln F}{\partial \varphi}\bigg|_{\varphi=\varphi_0}, \qquad \beta_0 = -\frac{1}{2}\frac{\partial^2 \ln F}{\partial \varphi^2}\bigg|_{\varphi=\varphi_0}. \tag{3.5}$$

The effective gravitational constant determining the attraction between two bodies as measured in a Cavendish experiment is

$$\tilde{G} = G(1 + \alpha_0^2), \tag{3.6}$$

where G is the bare gravitational constant entering the action. Furthermore, the Eddington parameterised PN parameters [82, 83] can be expressed exclusively in terms of α_0 and β_0 through

$$\beta^{\rm PPN} - 1 = \frac{\alpha_0^2\beta_0}{2(1+\alpha_0^2)^2}, \qquad \gamma^{\rm PPN} - 1 = -2\frac{\alpha_0^2}{1+\alpha_0^2}. \tag{3.7}$$

For an interpretation of these equations in terms of fundamental interactions, see [84]. In consequence, weak-field deviations from GR are completely determined by the Taylor expansion of $\ln F$ to quadratic order about $\lim_{r\to\infty}\varphi = \varphi_0$. For these reasons, most of the literature on ST theories has focused on coupling functions of quadratic form [33, 34] and we follow this approach by employing a coupling function

$$F = \exp\left[-2\alpha_0(\varphi - \varphi_0) - \beta_0(\varphi - \varphi_0)^2\right]. \tag{3.8}$$

The asymptotic value φ_0 does not represent an additional degree of freedom in the theory because it can be reabsorbed by a field redefinition $\varphi \to \varphi + \varphi_0$ [60] and we therefore set $\varphi_0 = 0$ without loss of generality in the rest of this paper[7]. We can furthermore assume $\alpha_0 \geqslant 0$ because the sign of α_0 is degenerate with the field redefinition $\varphi \to -\varphi$. Despite its apparent simplicity, this two-parameter family of ST theories is representative of all ST theories with the same phenomenology up to first PN order. Brans–Dicke theory [12] is a

[6] We introduce factors $-1/2$ in equation (3.5), and consequently a factor -2 in equation (3.8), to be consistent with previous studies, e.g., [13, 33, 34].

[7] The class of theories here parameterised by (α_0, β_0) can equivalently be represented using $F = \exp(-2\beta_0\varphi^2)$ but keeping φ_0 as an independent parameter, as done, e.g., in [33].

special case of equation (3.8) with the Brans–Dicke parameter (defined above equation (2.2)) given by $\omega_{\rm BD} = (1 - 6\alpha_0^2)/2\alpha_0^2$ and $\beta_0 = 0$. It is worth mentioning here that theories with the coupling function (3.8) and strictly vanishing potential have been shown to exhibit non-viable cosmological evolutions [85, 86]; however, this can be cured by introducing a suitable (sufficiently flat) potential which leaves the phenomenology on stellar scales unchanged [87, 88].

It is well known that all deviations in the structure of spherically symmetric bodies in ST theory from their general relativistic counterparts are given in terms of a series of PN terms proportional to α_0^2 [13, 89]; see also equation (3.7) above. Any ST theory with $\alpha_0 = 0$ is therefore perturbatively equivalent to GR and current observations (see below) constrain α_0 to be very small. In 1993, however, Damour and Esposito-Farèse [33, 34] discovered a remarkable non-perturbative effect called *spontaneous scalarisation*, which introduces macroscopic modifications to the structure of NSs even when α_0 is very small or vanishes [90]. For certain values $\beta_0 < 0$, there exists a threshold in the compactness (M/R, where M is the total mass of the object and R is its radius) of stellar structure at which spherically symmetric equilibrium solutions develop significant scalar hair. One can find three distinct solutions in this regime: besides a weakly scalarised solution where the ratio between the scalar charge and the star's mass ω/M is of the order of α_0, two strong-field solutions appear where this ratio is of order unity [51, 91]. If $\alpha_0 = 0$, the weak-field solution is a GR star and the two strong field solutions coincide. Notably, scalarised solutions are present for compactness values of order $M/R \gtrsim 0.2$ [89], as realised in NSs. When present, scalarised NSs can be energetically favoured over their weak-field counterparts [33, 34, 92], allowing for the possibility of dynamical transitions between the two branches of solutions [51]. Spontaneously scalarised stars have been found for $\beta_0 \lesssim -4.35$ [51, 91], but the exact value of this threshold depends on the EOS.

The (α_0, β_0) parameter space of ST theories has been severely constrained by observations. Solar System probes include measurements of Mercury's perihelion shift [93], Lunar laser ranging [94], light deflection measured with very-long-baseline interferometry [95], and the impressive bound $\alpha_0 < 3.4 \times 10^{-3}$ obtained with the Cassini space mission [61]. Timing of binary pulsars currently provides the tightest constraints in the β_0 direction of the parameter space [96]. In particular, observations from pulsars PSR J1738 + 0333 [97] and PSR J0348 + 0432 [98] (both orbiting a white dwarf companion) rule out a wide range of theories exhibiting prominent spontaneous scalarisation. Current observational constraints are summarised in figure 1 where the shaded area is now excluded. Note, however, that the binary-pulsar constraints apply to the case of a single massless scalar field. ST theories with multiple scalar fields [43] or with one massive field [99] may still lead to spontaneously scalarised NSs over a wide range of the theories' parameters without coming into conflict with the binary pulsar observations.

3.3. Initial profiles

We perform simulations of stellar collapse starting from two types of initial data: (i) polytropic models generated in the static limit of the ST theory equations and (ii) 'realistic' SN progenitors obtained from stellar evolutionary computations performed by Woosley and Heger [100].

(i) In the static limit, the evolution equations presented in sections 2.2.1–2.2.3 reduce to (see [33, 43])

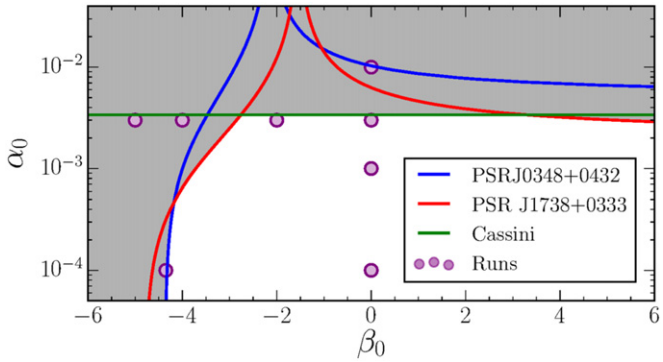

Figure 1. Experimental constraints on the ST-theory parameters (α_0, β_0) entering the coupling function F. The shaded area is currently ruled out by observations; GR lies at $\alpha_0 = \beta_0 = 0$. The most stringent constraints on α_0 are provided by the Cassini space mission while the binary-pulsar experiments impose strong bounds on β_0. Circles mark our choices for (α_0, β_0) used in section 5. This figure is produced using the data published in figure 6.3 of [1].

$$\partial_r \Phi = FX^2\left(\frac{m}{r^2} + 4\pi r\frac{P}{F^2} + \frac{r}{2F}\eta^2\right), \tag{3.9}$$

$$\partial_r m = 4\pi r^2\frac{\rho h - P}{F^2} + \frac{r^2}{2F}\eta^2, \tag{3.10}$$

$$\partial_r P = -\rho h F X^2\left(\frac{m}{r^2} + 4\pi r\frac{P}{F^2} + \frac{r}{2F}\eta^2\right) + \rho h\frac{F_{,\varphi}}{2F}X\eta, \tag{3.11}$$

$$\partial_r \varphi = X\eta, \tag{3.12}$$

$$\begin{aligned}\partial_r \eta = &-2\frac{\eta}{r} - 2\pi X\frac{\rho h - 4P}{F^2}F_{,\varphi} \\ &- \eta F X^2\left(\frac{m}{r^2} + 4\pi r\frac{P}{F^2} + \frac{r}{2F}\eta^2\right) + \frac{X}{2}\frac{F_{,\varphi}}{F}\eta^2,\end{aligned} \tag{3.13}$$

which generalise the Tolman–Oppenheimer–Volkoff [101, 102] equations to ST theory. As in GR, the equation for the metric potential Φ decouples from the remainder and we need an EOS $P = P_{\rm EOS}(\rho)$ to close the system.

In practice, we integrate the system (3.9)–(3.13) outwards starting at the origin where boundary and regularity conditions require

$$\begin{aligned}&\Phi(0) = 0, \quad m(0) = 0, \quad P(0) = P_{\rm EOS}(\rho_{\rm c}), \\ &\varphi(0) = \varphi_{\rm c}, \quad \eta(0) = 0.\end{aligned} \tag{3.14}$$

Here, $P_{\rm c}$ (or, alternatively, $\rho_{\rm c}$) is a free parameter determining the overall mass and size of the star and the central value of the scalar field $\varphi_{\rm c}$ is related through the integration to the value of φ at infinity. In our case, the boundary condition for the scalar field is $\varphi(r \to \infty) = \varphi_0 = 0$ and the task is to identify the 'correct' central value $\varphi_{\rm c}$ that satisfies the outer boundary condition. From a numerical point of view, this task represents a *two point boundary value problem* [103] and we use a *shooting algorithm* to solve it. For this purpose, we note that the integration terminates at the stellar surface $r_{\rm s}$ defined as the innermost radius where $P = 0$. From this radius $r_{\rm s}$, we could in principle

continue the integration to infinity by setting the matter sources to zero and switching to a compactified radial coordinate such as $y \equiv 1/r$. We have found such a scheme to work successfully [43], but here we implement an equivalent, but conceptually simpler algorithm. The numerical solution computed for $r \leqslant r_{\rm s}$ can be matched to a vacuum solution at $r > r_{\rm s}$ to relate the scalar field at the stellar surface $\varphi_{\rm s}$ to its asymptotic value φ_0 at $r = \infty$ [33]:

$$\varphi_{\rm s} = \varphi_0 - \frac{X_{\rm s}\eta_{\rm s}}{\sqrt{(\partial_r\Phi_{\rm s})^2 + X_{\rm s}^2\eta_{\rm s}^2}}\operatorname{arctanh}\frac{\sqrt{(\partial_r\Phi_{\rm s})^2 + X_{\rm s}^2\eta_{\rm s}^2}}{\partial_r\Phi_{\rm s} + 1/r_{\rm s}}, \tag{3.15}$$

where the subscript s denotes quantities evaluated at $r_{\rm s}$. The shooting algorithm starts the integration of equations (3.9)–(3.13) with some initial guess $\varphi(0)$, obtains the corresponding $\varphi_{\rm s}$ and then iteratively improves the choice of $\varphi(0)$ until it leads to a $\varphi_{\rm s}$ that satisfies equation (3.15) within some numerical tolerance (10^{-10} for the absolute difference in our case).

The central density or pressure can be freely chosen and parameterises the family of static solutions for a given ST theory (α_0, β_0) in the same way as it does in GR. The members of this one-parameter family of solutions are often characterised by their total gravitational mass which is given by [33]

$$m_\infty = r_{\rm s}^2\partial_r\Phi_{\rm s}\sqrt{1 - \frac{2m_{\rm s}}{r_{\rm s}}} \times \exp\left[-\frac{\partial_r\Phi_{\rm s}}{\sqrt{(\partial_r\Phi_{\rm s})^2 + X_{\rm s}^2\eta_{\rm s}^2}}\operatorname{arctanh}\frac{\sqrt{(\partial_r\Phi_{\rm s})^2 + X_{\rm s}^2\eta_{\rm s}^2}}{\partial_r\Phi_{\rm s} + 1/r_{\rm s}}\right]. \tag{3.16}$$

All polytropic initial profiles used in this work are generated using a polytropic EOS $P = K\rho^\Gamma$ with $K = 4.9345 \times 10^{14}$ [cgs], $\Gamma = 4/3$ and central mass density $\rho_{\rm c} = 10^{10}$ g cm^{-3}; these parameters are considered qualitatively reasonable approximations to model iron cores supported by the degeneracy pressure of relativistic electrons [76]. In particular, the choice $\rho_{\rm c} = 10^{10}$g cm^{-3} results in stars with baryonic mass $\sim 1.44 M_\odot$, slightly below the Chandrasekhar limit [29].

(ii) We also perform core collapse simulations using more realistic pre-SN models. Woosley and Heger [100] evolved non-rotating single stars up to the point of iron core collapse [104, 105]. Here, we consider two specific models of their catalogue obtained from the evolution of stars with ZAMS mass $M_{\rm ZAMS} = 12M_\odot$ and $40M_\odot$. We refer to these models as WH12 and WH40 respectively. Model WH12 has a steep density gradient outside its iron core, which results in a low accretion rate after bounce. Even if no explosion occurs, the delay to BH formation would be multiple seconds and no BH forms over the time we simulate. Model WH40, on the other hand, has a very shallow density gradient, resulting in a high accretion rate after bounce. This pushes the protoneutron star over its maximum mass and leads to BH formation within a few hundred milliseconds of bounce (see [26]). Hence, we use model WH12 to explore ST theory for a scenario in which core collapse results in a stable NS and model WH40 for a scenario in which the protoneutron star collapses to a BH.

Since WH12 and WH40 are Newtonian models, we initialise the scalar-field variables φ, ψ and η to 0. An unfortunate consequence of this artificial (but unavoidable) approximation is that no scalar-field dynamics occur at all if $\alpha_0 = 0$: all source terms on the right-hand side of equations (2.26)–(2.28) vanish at all times, and the evolution

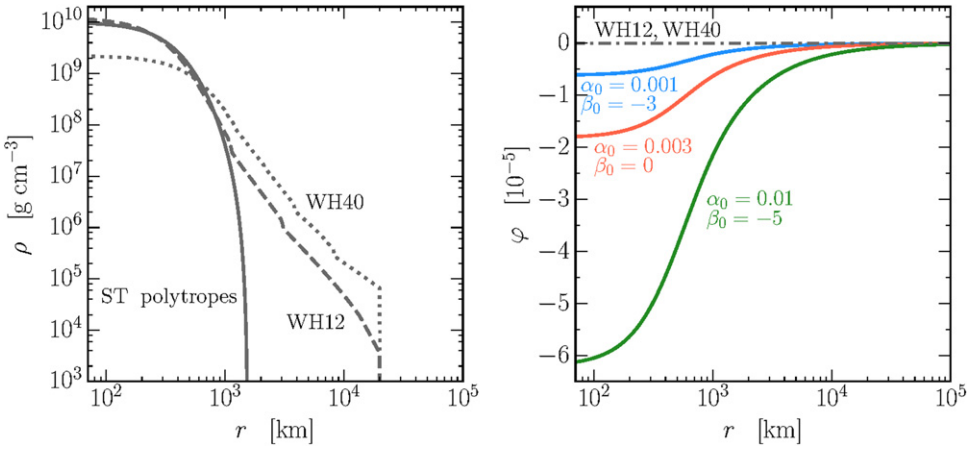

Figure 2. Mass–density (left panel) and scalar-field (right panel) profiles for the initial data considered in this study. In particular, dashed and dotted lines show the $M_{\rm ZAMS} = 12M_\odot$ (WH12) and $M_{\rm ZAMS} = 40M_\odot$ (WH40) pre-SN models of Woosley and Heger [100] while the solid lines show three $\Gamma = 4/3$ polytropes generated in ST theories with $(\alpha_0, \beta_0) = (0.001, -3)$, $(0.003, 0)$, $(0.01, -5)$. The mass–density distributions of all three ST polytropes are indistinguishable from their GR counterparts. The more realistic models WH12 and WH40 mostly differ from the polytropic ones through the presence of outer low-density layers. Note that we cut the WH models at $r_{\rm s} = 2 \times 10^4$ km and pad them with an artificial atmosphere of $\rho_{\rm atm} = 1$ g cm^{-3}. The scalar field is more pronounced in models with higher α_0, but the low compactness of these models prevents spontaneous scalarisation. The scalar field is initialised to zero when the WH models are evolved.

proceeds exactly as in GR. We overcome this problem, by using small but non-zero values for α_0, which triggers a brief initial transient in the scalar field that afterwards settles down into a smooth but non-trivial configuration eventually leading to significant scalar field dynamics as the collapse progresses through increasingly compact stages of the core.

For both classes of initial data there remains one degree of freedom that we need to specify: the metric function Φ is determined by equation (3.9) only up to an additive constant. While our integration in case (i) starts with $\Phi(0) = 0$, we can trivially shift the profile of $\Phi(r)$ by a constant (leaving all other variables unchanged) and still have a solution of the system of equations (3.9)–(3.13). We use this freedom to enforce that the physical metric component $g_{tt} = 1$ as $r \to \infty$, so that coordinate time is identical to the proper time measured by an observer at infinity. In practice, this is achieved by using very large grids and fitting $\Phi = \Phi_0 + \Phi_1/r$ on the outer parts. Φ_0 is then the constant we subtract from the entire profile $\Phi(r)$. The realistic initial models of case (ii) above are calculated without a scalar field and in that case our procedure is equivalent to the standard matching in GR based on the Birkhoff theorem.

For illustration, we show in figure 2 some of the initial profiles used in this study. Because of the low compactness of iron cores, the polytropic profiles for all values of $\alpha_0 \leqslant 0.01$ present very similar mass–density distributions which also very closely resemble their GR counterpart. The magnitude of the scalar field inside the star increases as larger values are chosen for α_0 (see right panel of figure 2) while outside the star φ rapidly approaches the $1/r$ behaviour of equation (2.29). In the left panel of figure 2, we also see that

the realistic pre-SN models WH12 and WH40 are well approximated by a $\Gamma = 4/3$ polytrope in their central regions $r \lesssim 10^3$ km; outer less degenerate layers of lighter elements, however, substantially broaden the mass–density distribution outside the iron core.

In order to overcome instabilities arising in our numerical scheme due to zero densities ρ [54], we add an artificial atmosphere outside the stellar surface r_s. More specifically, we pad the polytropic profiles with a layer of constant mass density $\rho_{\rm atm} = 1\,{\rm g\,cm^{-3}}$. The WH models are cut at $r_s = 2 \times 10^4$ km (see figure 2) and padded with an artificial atmosphere of $\rho_{\rm atm} = 1\,{\rm g\,cm^{-3}}$. By comparing evolutions using different values for the atmospheric density, we find the atmosphere to be completely irrelevant to the dynamics of the star, but we observe that significantly larger values than $\rho_{\rm atm} = 1\,{\rm g\,cm^{-3}}$ unphysically affect the propagation of the scalar wave signal such that the wave signal does not converge in the limit of large extraction radii. We estimate the resulting error for our choice by comparison with otherwise identical simulations using instead $\rho_{\rm atm} = 10\,{\rm g\,cm^{-3}}$; the observed differences are $|\Delta h(t)|/h(t) \sim 0.3\%$ in the extracted waveform (see equation (3.23) below).

3.4. GW extraction and detector sensitivity curves

The output of a GW detector $s(t) = n(t) + h(t)$ is the sum of noise $n(t)$ and signal $h(t)$. For quadrupole GWs, as present in GR, $h(t)$ is related to the metric perturbation $h_{+,\times}$ in the transverse traceless gauge through the beam pattern functions $A_{+,\times}$: $h(t) = A_+ h_+(t) + A_\times h_\times(t)$ [106]. Monopole GWs are present in ST theory and are related to the dynamics of the scalar field φ. In this case, the detector response $h(t) = A_\circ h_\circ(t)$ is given by the metric perturbation $h_\circ(t)$ weighted by the correspondent beam pattern $A_\circ$ [107, 108] [8]. If we denote by $\tilde{h}(f)$ and $\tilde{n}(f)$ the Fourier transform of $h(t)$ and $n(t)$, respectively, the (one-sided) noise power spectral density $S_n(f)$ is defined as

$$\langle \tilde{n}(f)\tilde{n}^*(f')\rangle = \frac{1}{2}\delta(f-f')S_n(f), \tag{3.17}$$

where $\langle\cdot\rangle$ denotes a time average for stationary stochastic noise. The signal-to-noise ratio is defined as (see [109] where the numerical factor is derived; see also [110])

$$\rho^2 = \int_0^\infty \frac{4\,|\tilde{h}(f)|^2}{S_n(f)}{\rm d}f. \tag{3.18}$$

The characteristic strains for noise and signal are defined as

$$h_n(f) = \sqrt{f S_n(f)}, \qquad h_{\rm c}(f) = 2f|\tilde{h}(f)| \tag{3.19}$$

such that ρ^2 can be written as the squared ratio between signal and noise:

$$\rho^2 = \int_{-\infty}^{+\infty}\left[\frac{h_{\rm c}(f)}{h_n(f)}\right]^2 {\rm d}\ln f. \tag{3.20}$$

The most common convention used to display detector sensitivity curves involves plotting the square root of the power-spectral density

$$\sqrt{S_n(f)} = \frac{h_n(f)}{\sqrt{f}}; \tag{3.21}$$

[8] The most sensitive directions corresponding to A_+, $A_\times$ and $A_\circ$ are all different from each other. If only these three polarisations are present, a network of four detectors can in principle disentangle them and estimate the source direction [48]. Note also that optimally oriented sources correspond to $A_+ = 1$, $A_\times = 1$ but $A_\circ = 1/2$ [107, 108].

and the analogous quantity [109]

$$\sqrt{S_h(f)} = \frac{h_c(f)}{\sqrt{f}} = 2\sqrt{f}\,|\tilde{h}(f)|, \tag{3.22}$$

which characterises the GW signal[9]. In the following we will use sensitivity curves $\sqrt{S_n(f)}$ for:

(i) the Advanced LIGO detectors [55, 56] in their zero-detuned high-power configuration, as anticipated in [111];
(ii) the proposed Einstein telescope [57], using the analytic fit reported in [110].

Scalar waves are also promising sources for future GW experiments targeting the deci-Hertz regime, such as the proposed space mission DECIGO [112].

In contrast to GR, ST theories admit gravitational radiation in spherical symmetry, specifically in the form of a radiative monopole of the scalar field or, equivalently, a so-called *breathing mode* when considering the Jordan frame. The metric perturbation of a monopole scalar wave in ST theory is [13]

$$h_\circ(t) = \frac{2}{D}\alpha_0 r(\varphi - \varphi_0), \tag{3.23}$$

where D is the distance between the detector and the source and the scalar field φ is evaluated at radius r. The factor α_0 is due to the coupling between the scalar field and the detector and limits the potential of GW observations to constrain ST theories [113]. Throughout this paper we consider optimally oriented sources, such that $h(t) = A_\circ h_\circ(t) = h_\circ(t)/2$ [107, 108].

In analysing our simulations, we proceed as follows. At a given radius $r_{\rm ext}$, we extract $\varphi(t)$ and compute $h(t)$. In order to eliminate the brief unphysical transient (see section 4.1), we truncate this early part from the time domain waveform $h(t)$. We then obtain $\tilde{h}(f)$ numerically using a fast Fourier transform (FFT) algorithm. To reduce spectral leakage, the FFT algorithm is applied to data $h(t)$ mirrored about the latest timestep available and the result $\tilde{h}(f)$ is normalised accordingly [114]. This confines spectral leakage to frequencies $f \gtrsim 200$ Hz (see the tails in figures 7 and 8) where the signal is very weak. Finally, we compute $\sqrt{S_h(f)}$ from equation (3.22) and compare it with the detectors' sensitivity curves $\sqrt{S_n(f)}$.

4. Numerical implementation

In this section, we provide details of our numerical scheme, stressing the modifications needed in ST theories with respect to the GR version of the code (section 4.1). We present the convergence properties in section 4.2.

4.1. Second-order finite differences and high-resolution shock capturing

Our numerical code is built on top of GR1D, an open-source spherically symmetric FORTRAN 90 + code developed by O'Connor and Ott [54]. GR1D has been applied to a range of problems in stellar collapse and BH formation (e.g., [26, 115]). Its most recent GR version is available at [116] and includes energy-dependent neutrino radiation transport [117].

As in the GR case, the constraint equations (2.21) and (2.22) for the metric functions Φ and m are integrated using standard second-order quadrature. In the scalar-field

[9] The convention for $\sqrt{S_h(f)}$ used in [50] differs by a factor 2 when compared to those of [109] used here.

equations (2.26)–(2.28), the source terms are discretised using centred second-order stencils. Due to the potential formation of shocks in the matter variables, their evolution is handled with a high-resolution shock capturing scheme as described in detail in section 2.1 of [54]. For our evolutions in ST theory, we extended the flux and source terms of GR1D in accordance with our equations (2.34)–(2.39). Integration in time of the evolution equations for the matter and scalar fields is performed using the method of lines with a second-order Runge–Kutta algorithm. One significant difference from the GR case arises from the presence of the scalar field as a dynamical degree of freedom with the characteristic speed of light, whereas in spherical symmetry in GR we only have to consider the characteristic speed of sound for the matter degrees of freedom (see section 2.2.3). In order to satisfy the Courant–Friedrichs–Lewy stability condition we therefore determine the timestep using the speed of light instead of the speed of sound, which results in smaller values for the allowed timestep as compared with the corresponding evolutions in GR.

As discussed in section 2.2.3, a key ingredient in the implementation of shock capturing methods is the use of a system of evolution equations in flux conservative form which is available in terms of the conserved variables D, S^r, τ but not in the primitive variables ρ, v and ϵ. The primitive variables appear in the constraint equations for the metric, the flux terms of the shock-capturing scheme, in the EOS, and also form convenient diagnostic output. Conversion between the two sets of variables is thus required at each timestep. This process is straightforward for the direction primitive $\rightarrow$ conserved; see equations (2.17)–(2.19). The reverse transformation, however, is non-trivial because of the presence of the pressure P which is an intrinsic function of ρ and ϵ given by the EOS. This conversion is performed iteratively using a Newton–Raphson algorithm: given an initial guess $\hat{P}$ for the pressure from the previous timestep, we first calculate in this order

$$v = \frac{S^r}{\tau + \hat{P}/F^2 + D}, \tag{4.1}$$

$$\rho = \frac{F^{3/2}D}{X}\sqrt{1 - v^2}, \tag{4.2}$$

$$\epsilon = h - \frac{\hat{P}}{\rho} - 1 = \frac{F^2(\tau + D)(1 - v^2) - \hat{P}v^2}{\rho} - 1. \tag{4.3}$$

Then we compute an updated estimate for the pressure from the EOS $P = P(\rho, \epsilon)$, and iterate this procedure until convergence.

The evolution of the scalar field turns out to be susceptible to numerical noise near the origin $r = 0$, which represents a coordinate singularity. In order to obtain long-term stable evolutions, we add artificial dissipation terms of Berger–Oliger type [118] to the scalar evolution equations. Specifically, we add a dissipation term of the form $\mathcal{D} \times \Delta r^4 \times \partial^4 u/\partial r^4$ to the right-hand side of equations (2.26)–(2.28), where u stands for either of the scalar-field variables, Δr is the width of the grid cell, and $\mathcal{D}$ is a dissipation coefficient. In practice, we obtain good results using $\mathcal{D} = 2$.

In all our simulations, the grid functions exhibit much stronger spatial variation in the central region of the star than in the wave zone. In order to accommodate these space dependent requirements on the resolution of our computational domain, we use a numerical domain composed of an inner grid with constant and an outer grid with logarithmic spacing. This setup enables us to capture the dynamics of the inner core with high accuracy while maintaining a large grid for GW extraction at tolerable computational cost. Unless specified otherwise, we use the following grid setup. The outer edge of the grid is placed at

$R_{\rm out} = 1.8 \times 10^5$ km and the two grid components are matched at $R_{\rm match} = 40$ km. The cell width of the inner grid is $\Delta r = 0.25$ km. The total number of zones is set to $N_{\rm zones} = 5000$, such that 160 (4840) zones are present in the inner (outer) grid. Four ghost cells are added at both $r = 0$ and $r = R_{\rm out}$ for implementing symmetry and boundary conditions. GW signals are extracted at $r_{\rm ext} = 3 \times 10^4$ km, which is well outside the surface of the star but sufficiently far from the outer edge of the grid $R_{\rm out}$ to avoid contamination from numerical noise from the outer boundary. We simulate the evolution for 0.7 s to allow for the entire GW signal to cross the extraction region.

Radial gauge, polar slicing coordinates are not well adapted to BH spacetimes: as the star approaches BH formation, the lapse function α tends to zero in the inner region [119] and inevitably introduces significant numerical noise. The stellar evolution, however, is effectively frozen as $\alpha \to 0$. Following Novak [50], we handle BH formation by explicitly stopping the evolution of the matter variables while we let the scalar field propagate outwards. In practice, we freeze the matter evolution whenever the central value of α becomes smaller than $\alpha_T = 5 \times 10^{-3}$. By varying the threshold α_T over two orders of magnitude, we verified this procedure introduces a negligible error $|\Delta\varphi|/\varphi \lesssim 1\%$ on the extracted wave signal in case of BH formation.

A final note on the numerical methods concerns the time window used for the wave extraction. As mentioned in section 3.2, our initial data for the realistic progenitor models require us to trigger scalar dynamics by using a small but non-zero value for α_0 that induces a brief transient in the wave signal. This transient is not part of the physical signal we are interested in and is removed by calculating waveforms in an interval starting not at zero retarded time, but shortly afterwards: we use for this purpose the time window $[t_i, t_f]$ with $t_i = r_{\rm ext}/c + 0.006$ s to $t_f = r_{\rm ext}/c + 0.6$ s from the beginning of the simulation. This provides us with waveforms of total length $\Delta t \sim 0.6$ s corresponding to a lower bound $f \sim 1.7$ Hz in the frequency domain. Note that our waveforms are significantly longer than those obtained in previous studies of collapse in ST theories [52].

4.2. Self-convergence test

Here we present the convergence properties of our dynamical code. Given three simulations of increasing resolutions with grid spacings $\Delta r_1 > \Delta r_2 > \Delta r_3$, the self-convergence factor Q of a quantity q is defined by

$$Q = \frac{q_1 - q_2}{q_2 - q_3} = \frac{(\Delta r_1)^n - (\Delta r_2)^n}{(\Delta r_2)^n - (\Delta r_3)^n}, \tag{4.4}$$

where q_i indicates the quantity q obtained at resolution Δr_i and n is the convergence order of the implemented numerical scheme.

We collapse a $\Gamma = 4/3$ polytropic core in ST theory with $\alpha_0 = 10^{-4}$ and $\beta_0 = -4.35$ using the hybrid EOS with $\Gamma_1 = 1.3$, $\Gamma_2 = 2.5$ and $\Gamma_{\rm th} = 1.35$. This model is evolved for three uniformly spaced[10] grids of size $R_{\rm out} = 2 \times 10^3$ km with $N = 6000$, 12 000 and 24 000 grid cells. For these grids, we expect $Q = 2$ ($Q = 4$) for first- (second-) order convergence. The bottom panels of figure 3 show the convergence properties of the gravitational mass m and the scalar field φ at various timesteps. Solid lines show the difference between the coarse and the medium resolution runs $q_1 - q_2$; dashed (dotted) lines show the difference between the medium and the fine resolution runs $q_2 - q_3$ multiplied by the expected first- (second-) order

[10] For the convergence analysis, we use uniform grids exclusively, i.e. do not switch to a logarithmic spacing in the outer parts. Nonlinear grid structure would make a quantitative convergence analysis highly complicated.

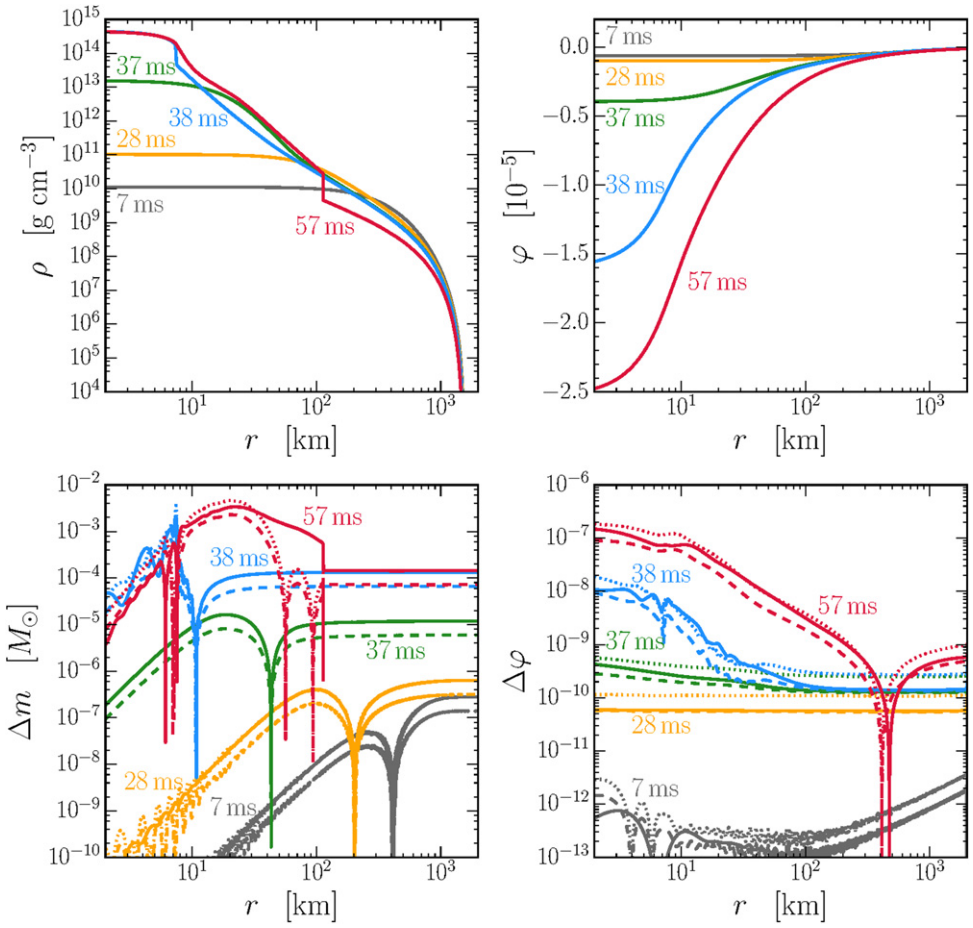

Figure 3. Convergence test of stellar collapse in ST theory with $\alpha_0 = 10^{-4}$ and $\beta_0 = -4.35$. A polytropic core is collapsed using the fiducial hybrid EOS for three different resolutions (see text for details). The top panels show the evolution of the mass density ρ (left) and the scalar-field φ (right) for the highest-resolution run a $t = 7$ (grey), 28 (yellow), 37 (green), 38 (blue), 57 (red) ms after starting the simulations. Bounce happens at $t \sim 38$ ms and the shock reaches the surface of the star at $t \sim 131$ ms. The bottom panels show the self-convergence properties of the gravitational mass m (left) and the scalar field φ (right) at the same times. As detailed in the text, solid and dotted (dashed) lines are expected to coincide for second- (first-) order convergence. We initially observe second order convergence which decreases to first order due to (i) the shock capturing scheme when a discontinuity forms at bounce and (ii) numerical noise in the scalar field propagating in from the outer boundary.

self-convergence factor $Q = 2$ ($Q = 4$). Second-order convergence is achieved if the solid and dotted lines coincide, while the code is only first-order convergent if the solid and dashed lines coincide. The evolution of ρ and φ is displayed in the top panels for orientation.

The enclosed gravitational mass m shows good second-order convergence properties before bounce $t \lesssim 38$ ms, while convergence deteriorates to first order as the shock propagates outwards at $t \gtrsim 38$ ms. This is a characteristic feature of high-resolution shock-capturing schemes; they are second-order (or higher) schemes for smooth fields, but become first-

order accurate in the presence of discontinuities [54]. Note that the behaviour of the total gravitational and baryonic mass is more complex than in the GR limit where both are conserved because of the absence of gravitational radiation in spherical symmetry and the vanishing of the source term s_D in equation (2.37). The convergence properties of the scalar field are more complicated. While evolved with a second-order accurate scheme, we observe that the scalar field's convergence may deteriorate for the following two reasons: (i) the drop to first-order convergence of the matter fields which source the scalar dynamics; (ii) numerical noise generated at the outer boundary, especially during the early transient (note that in this convergence analysis the outer boundary is located much closer to the core than in our production runs because of the limit imposed by a strictly uniform grid). The observed convergence in the scalar field bears out these effects. Initially convergent at second order, we note a drop to roughly first order after one light crossing time $R_{\rm out}/c \sim 7$ ms. As the noise is gradually dissipated away, the convergence increases back towards second order, but drops once more to first order at the time the shock forms in the matter profile around 38 ms.

We also tested the convergence of the scalar waveform $\varphi(t)$ extracted at finite radius in these simulations and observe first-order convergence which we attribute to the relatively small total computational domain such that the outer boundary effects discussed above causally affect the extraction radius early in the simulation. The resulting uncertainty in the waveform is obtained by comparing the finite resolution result with the Richardson extrapolated (see, e.g., [120]) waveform. We find a relative error of 10% which we regard as a conservative estimate since the production runs have much larger computational domains.

5. Results and discussion

In this section, we present the results of our simulations. After illustrating the main features of stellar collapse in ST theories (section 5.1), we present our predictions for monopole gravitational radiation (section 5.2). All waveforms presented in this section are publicly available at [58].

5.1. Core-collapse dynamics

The main features of the core-collapse dynamics are summarised in figures 4 and 5. We present the collapse of both a polytropic core and two realistic pre-SN models (section 3.3) in ST theory with $\alpha_0 = 10^{-4}$ and $\beta_0 = -4.35$. These parameter choices lie on the edge of the parameter space region compatible with binary pulsar experiments (see figure 1) and marginally allow for spontaneous scalarisation [51, 91]. Collapse is performed using the hybrid EOS (section 3.1) with fiducial values $\Gamma_1 = 1.3$, $\Gamma_2 = 2.5$ and $\Gamma_{\rm th} = 1.35$.

Since $\Gamma_1 < 4/3$, the initial iron cores are not equilibrium solutions of the evolution equations and collapse is triggered dynamically. While the polytropic profile collapses smoothly from the very beginning of the simulation, a brief transient in the scalar-field evolution is present in the early stages of the collapse of both the WH12 and WH40 models. As already mentioned in section 3.3, this is due to the fact that these initial models are Newtonian and their initially vanishing scalar profiles are not fully consistent with the ST theory used in the evolution. This transient generates a pulse in the scalar field propagating outwards at the speed of light. The scalar field quickly settles down in the stellar interior while the spurious pulse reaches the outer edge of the grid at $R_{\rm out}/c \sim 0.6$ s where it is absorbed by the outgoing boundary condition.

As the collapse proceeds in either of the three models, the central mass density increases from its initial value up to beyond nuclear densities $\rho_{\rm nuc} \simeq 2 \times 10^{14}\,{\rm g\,cm^{-3}}$. The EOS

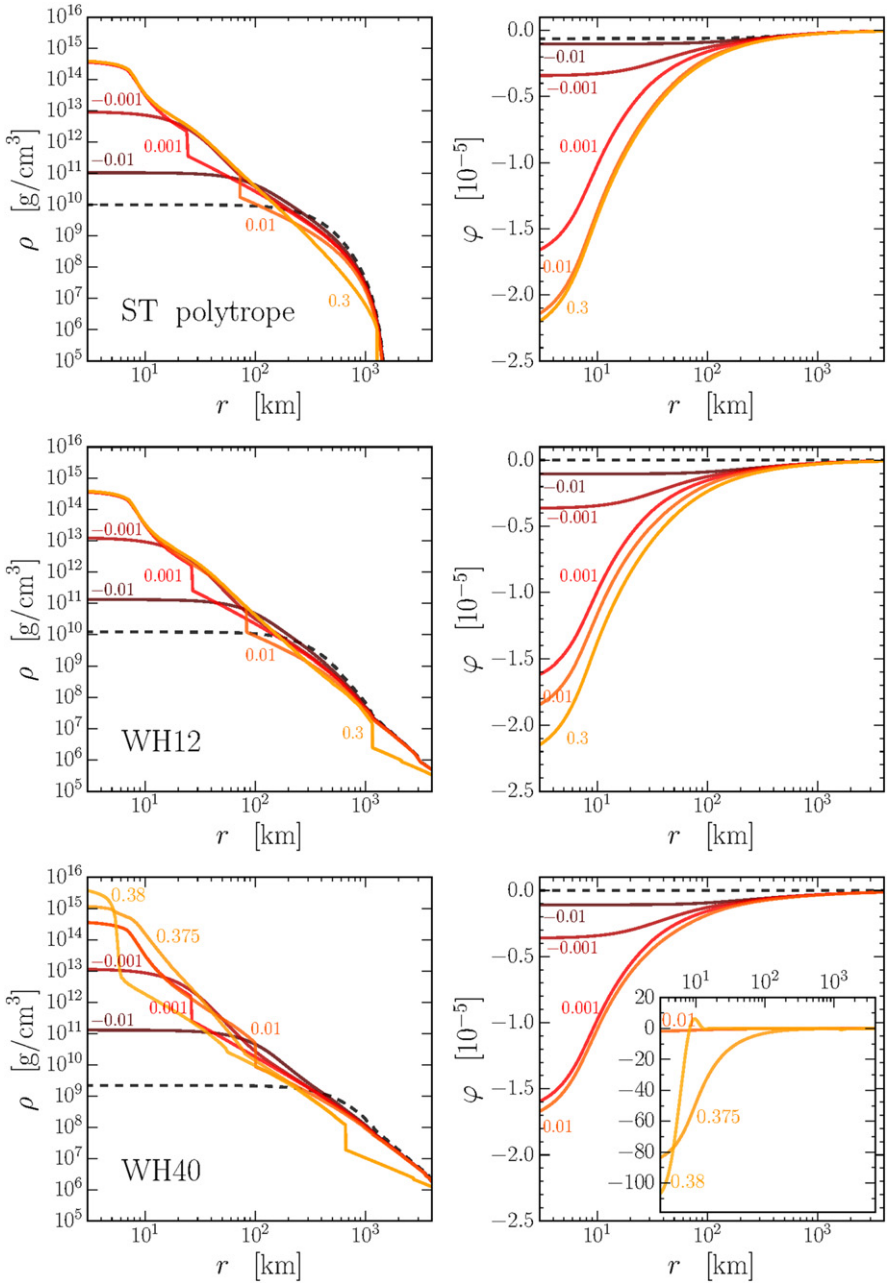

Figure 4. Collapse of a $\Gamma = 4/3$ polytrope (top), the $12M_\odot$ (centre) and $40M_\odot$ (bottom) pre-SN profiles of [100] in ST theory with $\alpha_0 = 10^{-4}$ and $\beta_0 = -4.35$, assuming $\Gamma_1 = 1.3$, $\Gamma_2 = 2.5$ and $\Gamma_{\rm th} = 1.35$. The evolution of the mass density ρ (left) and the scalar field φ (right) is shown as a function of the radius r at various timesteps $t - t_{\rm B} = -0.01$, -0.001, 0.001, 0.1, 0.3, 0.375, 0.38 s, measured from the bounce time $t_{\rm B}$. Timesteps are coloured from darker (early times) to lighter (late times) solid lines as labelled; initial profiles are shown with black dashed lines. The inset in the bottom right panel shows the wide variation of the scalar field when a BH is formed. An animated version of this figure is available online at [58].

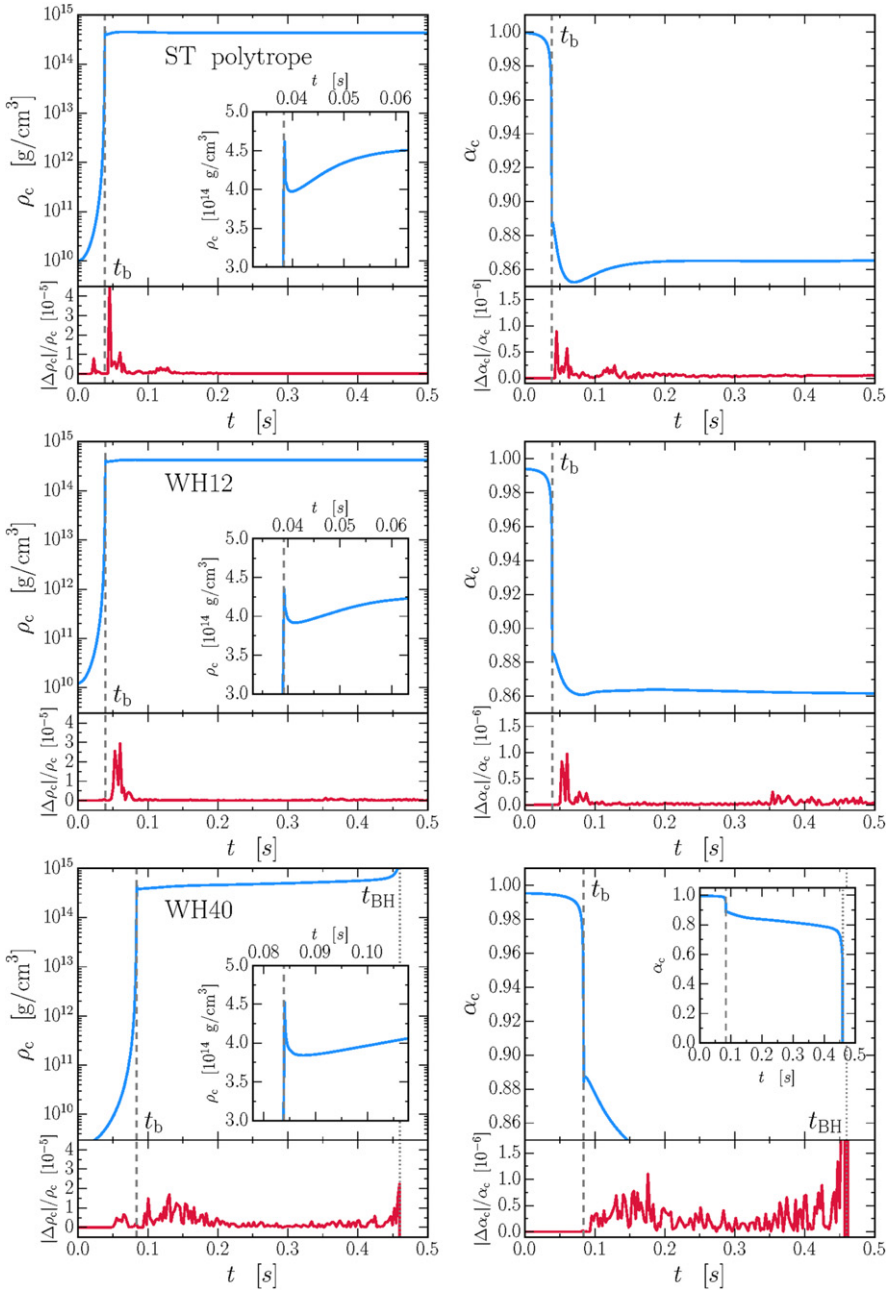

Figure 5. Evolution of the central values of the mass density ρ_c (left panels) and lapse function α_c (right panel) through collapse, bounce and late time evolution in ST theory with $\alpha_0 = 10^{-4}$ and $\beta_0 = -4.35$. We use the hybrid EOS with fiducial parameters ($\Gamma_1 = 1.3$, $\Gamma_2 = 2.5$ and $\Gamma_{th} = 1.35$) and three different initial profiles: ST polytrope (top), WH12 (centre) and WH40 (bottom). Grey dashed lines mark the bounce time t_b; the WH40 profile first collapses to a protoneutron star and then to a BH at $t_{BH} \sim 0.46$ s marked by grey dotted lines. Relative differences with analogous simulations performed in GR are shown in the lower subpanels (red lines). Deviations in the dynamics are very small: of the order of $|\Delta\rho_c|/\rho_c \sim 10^{-5}$ and $|\Delta\alpha_c|/\alpha_c \sim 10^{-6}$.

suddenly stiffens to an effective adiabatic index $\Gamma_2 \gg 4/3$ and the inner core bounces after $t_b \sim 38$, 39, and 84 ms from the beginning of the simulations, for the ST polytrope, WH12 and WH40 profile, respectively[11]. Core bounce launches a hydrodynamic shock into the outer core. Due to the steep density profile of the polytrope, the shock explodes the polytrope promptly, reaching its surface at ∼130 ms from the start of the simulation. Since we set $\Gamma_{\rm th} = 1.35$ to qualitatively account for reduced pressure due to nuclear dissociation and neutrino losses, the pressure behind the shock is not sufficient to lead to a prompt explosion of the more realistic WH12 and WH40 progenitors. The shock stalls and only secularly moves to larger radii as the accretion rate decreases. Core bounce is paralleled by a small reversal in the scalar field amplitude. For example, in the collapse of the polytropic model shown in figure 4, the central value of φ reaches a minimum $\sim -2.6 \times 10^{-5}$ at bounce before settling down to $\sim -2.3 \times 10^{-5}$. A more detailed description of the scalar field dynamics is postponed to section 5.2.

The inner regions of the promptly exploding polytropic model settle down to a stable compact remnant with compactness $m/r \sim 0.053$ (measured from the metric potential at $r = 10$ km). While simulations with model WH12 show that the shock stalls and then only slowly shifts to larger radii, the low accretion rate in this model does not increase its compactness above the values that we find for the polytropic model. In both models, the scalar charge ω evolves from $\sim -10^{-4}\, M_\odot$ to $\sim -2 \times 10^{-4}\, M_\odot$ during the entire evolution and thus remains of the order of $\omega/M \sim \alpha_0$, as predicted for weakly scalarised NS solutions (see section 3.2). In both simulations, the NSs do not evolve to strongly spontaneously scalarised solutions because the compactness of the core remains lower than the threshold at which multiple solutions appear ($m/r \sim 0.2$ [89]).

On the other hand, the WH40 model forms a protoneutron star that subsequently collapses to a BH within $t_{\rm BH} \sim 0.46$ s from the beginning of the simulation (∼0.38 s from bounce). The high accretion rate in this model quickly increases the central compactness. As BH formation is approached, our gauge choice causes the lapse function α to collapse to zero near the origin (figure 5) and the dynamics of the inner region effectively freezes. In this regime, spontaneously scalarised NS solutions are not only present but energetically favourable [33, 34, 92]. While collapsing towards a BH, the core first transits through a spontaneously scalarised NS. BH formation generates strong scalar-field excitation, enhanced in this case ($\beta_0 = -4.35$) by spontaneous scalarisation (see section 5.2.2). The central value $\varphi_{\rm c}$, which through collapse and bounce remains close to values of the order of $\sim -10^{-5}$, increases in magnitude to $\sim -2 \times 10^{-3}$. This signal propagates outwards at the speed of light, rapidly leaves the region of the stalled shock, and reaches the extraction radius after about ∼0.56 s from the beginning of the simulation.

Our gauge choice does not allow us to follow the evolution of the inner region of the star beyond BH formation. Following [50], we terminate the evolution of the matter variables at the onset of BH formation in order to ensure numerical stability. At this point, the inner core has reached a compactness of ∼0.466, close to the BH value of 0.5. We are still able to gain insight into the late-time behaviour of the scalar field, however, by solving the wave equation (2.8) on the now frozen background (see figure 4). We observe in these evolutions that, as the NS (now spontaneously scalarised) collapses to a BH, the scalar field slowly relaxes to a flat profile as predicted by the no-hair theorems [18–21, 121].

Overall, the entire dynamics strongly resembles GR. The scalar field is mostly driven by the matter evolution, which in turn is largely independent of the scalar field propagation. This point is illustrated in figure 5, where the central values of the mass density $\rho_{\rm c}$ and lapse

[11] The WH40 profile takes longer to reach $\rho_{\rm nuc}$ because of its lower initial central density (see figure 2).

function α_c obtained in ST theory and in GR are compared. The relative differences between these two scenarios are about $|\Delta\rho_c|\rho_c \sim 10^{-5}$ and $|\Delta\alpha_c|/\alpha_c \sim 10^{-6}$ throughout collapse, bounce, and (eventually) BH formation.

5.2. Monopole GW emission

Unlike GR, ST theories of gravity admit propagating monopole GWs. This breathing mode of the scalar field is potentially detectable with current and future GW interferometers which have therefore the potential of constraining the parameters of the theory. We now analyse the scalar GW signal extracted from our numerical simulations, separately discussing the effects of the EOS and the ST parameters.

5.2.1. Effect of the EOS. As detailed in section 3.1, the hybrid EOS is a simplified EOS model that qualitatively approximates more sophisticated microphysical EOS in the core collapse context (e.g., [77]). The hybrid EOS is characterised by three adiabatic indices for the pre-bounce dynamics (Γ_1), the repulsion at nuclear densities (Γ_2), and the response of the shocked material (Γ_{th}). The effect of the EOS on the emitted GW waveforms is explored in figure 6, where we show time-domain monopole waveforms $h(t) \propto r\varphi$ (see equation (3.23) with $\varphi_0 = 0$) for various choices of Γ_1, Γ_2, and Γ_{th}. All simulations shown in figure 6 are performed in ST theory with $\alpha_0 = 10^{-4}$ and $\beta_0 = -4.35$, the lower limit of β_0 compatible with present observations, using the WH12 and WH40 initial profiles. We plot the GW signals as a function of the retarded time $t - r/c$, such that the origin corresponds to a single light-crossing time at the extraction radius $r_{ext} = 3 \times 10^4$ km.

The structure of the emitted signals displayed in figure 6 consists of the following four main stages.

(i) The initial pulse of spurious radiation arises from the initialisation of the scalar field, as already pointed out in sections 3.3 and 5.1. This pulse propagates outwards and leaves the extraction region after a retarded time of about 0.006 s.

(ii) As the core collapses, the scalar field signal significantly grows in amplitude. Although the first ∼0.02 s of the waveform appear to be rather insensitive to the EOS, the adiabatic indices strongly affect the total amount of time the star spends in the collapse phase before bounce. In the hybrid EOS, this is controlled by Γ_1. Collapse is triggered by $\Gamma_1 \leqslant 4/3$ and the smaller Γ_1, the more rapid the collapse and the smaller the mass of the inner core that collapses homologously (e.g., [72, 74]). We note that in reality (and in simulations using more realistic microphysics), Γ_1 is not a parameter. Instead, the effective adiabatic index is a complex function of the thermodynamics and electron capture during collapse [74, 75]. Figure 6 shows that core bounce occurs in our simulations at retarded time $t - r_{ext}/c \sim 0.03, 0.04, 0.08$ s (0.06, 0.07, 0.14) for model WH12 (WH40) and $\Gamma_1 = 1.28, 1.3, 1.32$ respectively. The bounce itself is a rapid process with a duration of $\Delta t \sim$ 1–2 ms.

(iii) After bounce, the scalar field in the inner core settles down to a non-trivial profile, as illustrated in figure 4. The post-bounce value of φ at r_{ext}, hence the value of $h(t)$, encodes information about all three adiabatic indices. In particular, larger values of Γ_1 and smaller values of Γ_{th} both produce stronger wave signals $h(t)$, which can be intuitively understood as follows. Larger values of Γ_1 result in a more massive inner core in the pre-bounce stage because the speed of sound is larger and, hence, more matter remains in sonic contact in the central region. At bounce, this implies a more compact core and a correspondingly

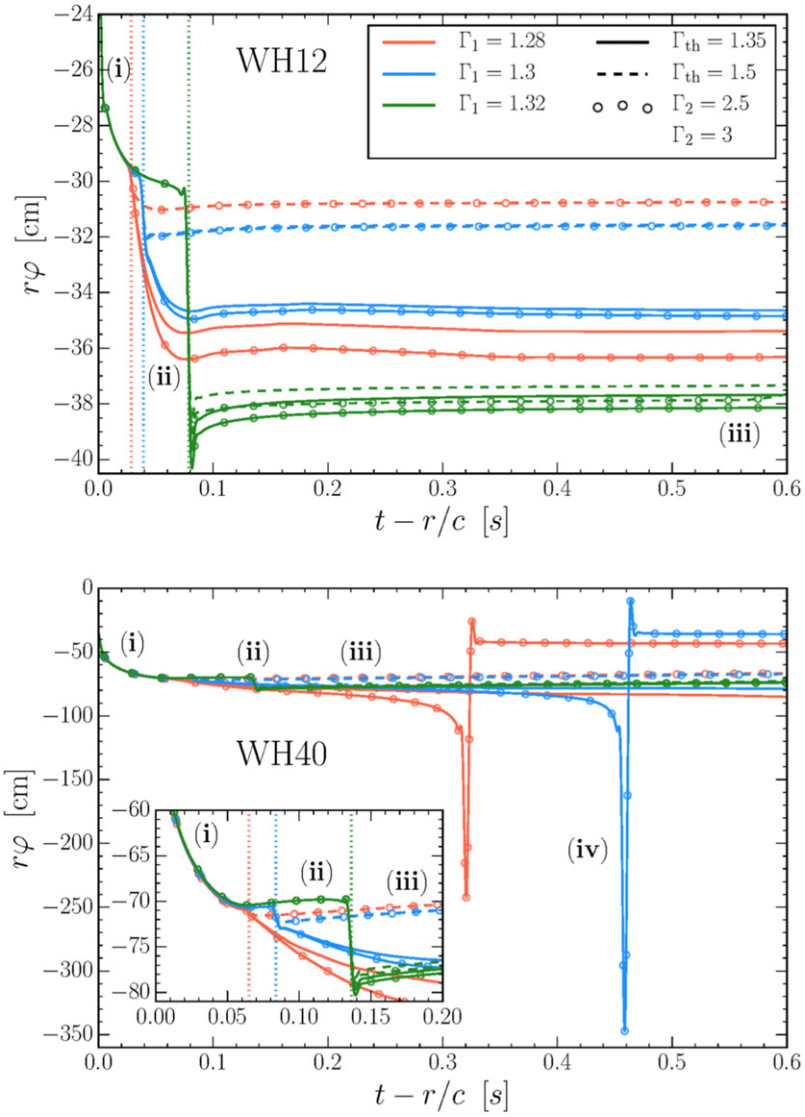

Figure 6. Effect of the hybrid EOS adiabatic indices on the emitted monopole gravitational waveform $h(t) \propto r\varphi$ (see equation (3.23)). The signal is plotted against the retarded time $t - r/c$ at the extraction radius. Simulations are performed using the preSN initial profiles WH12 (top) and WH40 (bottom) in ST theory with $\alpha_0 = 10^{-4}$ and $\beta_0 = -4.35$. The curves encode the value of Γ_1 in their brightness (colour) and the value of $\Gamma_{\rm th}$ in their line style: $\Gamma_1 = 1.28$ (red), 1.3 (blue), 1.35 (green); $\Gamma_{\rm th} = 1.35$ (solid), 1.5 (dashed). For each of these combinations, two curves are present: circles mark simulations with $\Gamma_2 = 2.5$, while no symbols are shown for $\Gamma_2 = 3$. For some cases, these two curves overlap to such high precision that they become indistinguishable in the plot. The lower-case Roman labels refer to the key phases of the GW signal described in section 5.2.1: (i) initial pulse of the spurious radiation; (ii) collapse and bounce; (iii) NS configuration; (iv) BH formation. The bounce time is marked with vertical dotted lines following the same colour codes of the other curves. Note that Γ_1 is the only adiabatic index that has an effect on the bounce time. Waveforms presented in this figure are available at [58].

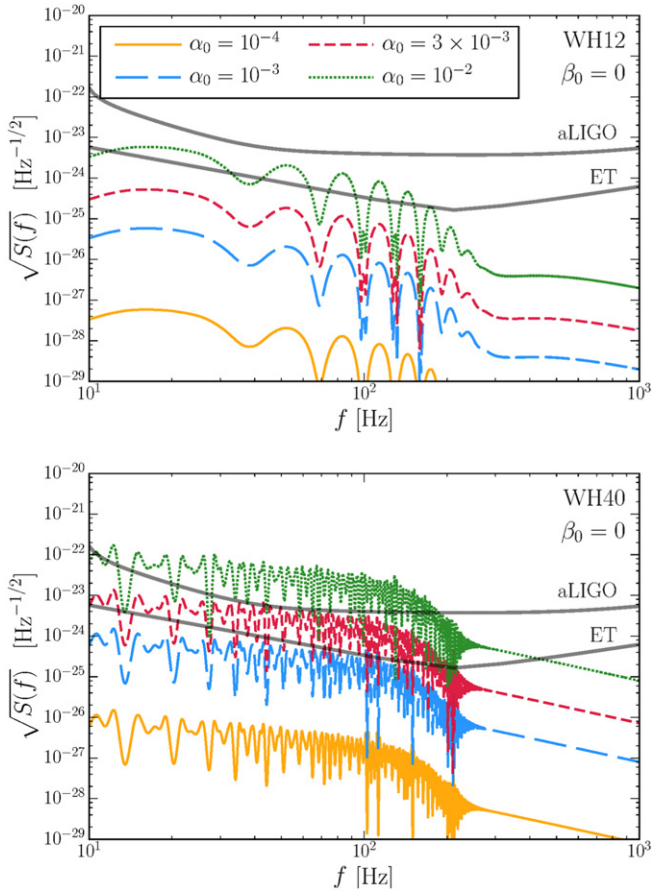

Figure 7. Effect of α_0 on frequency domain waveforms for monopole GWs emitted during stellar collapse. The $M_{\rm ZAMS} = 12M_\odot$ (top) and $40M_\odot$ (bottom) pre-SN models of [100] are evolved using the hybrid EOS with $\Gamma_1 = 1.3$, $\Gamma_2 = 2.5$ and $\Gamma_{\rm th} = 1.35$. Four simulations are presented for fixed $\beta_0 = 0$ (equivalent to Brans–Dicke theory): $\alpha_0 = 10^{-4}$ (orange, solid), 10^{-3} (blue, long-dashed), 3×10^{-3} (red, short-dashed), 10^{-2} (green, dotted). These values are compared with current experimental constraints in figure 1. We consider optimally oriented sources placed at $D = 10$ kpc and compare them with the expected sensitivity curves of Advanced LIGO and the Einstein telescope. Waveforms presented in this figure are available at [58].

larger amplitude in the scalar wave. Smaller values of $\Gamma_{\rm th}$ imply lower pressure in the shocked material, and, therefore, material that accretes through the shock settles faster onto the protoneutron star. In terms of microphysical processes, this effect is driven by neutrino cooling [74, 75], which is not included in our simulations. In contrast, we find that Γ_2 has a relatively minor effect on this phase of the wave signal: the scalar field profile is only slightly more pronounced for lower values of Γ_2, which result in a deeper bounce and a more compact postbounce configuration. Note that in the waveforms shown in figure 6, both $\Gamma_{\rm th}$ and Γ_2 only affect the wave signal at and after bounce. This is expected, since $\Gamma_{\rm th}$ only plays a role in the presence of shocked material and Γ_2 affects only the high density regime of the EOS not encountered in the collapse evolution prior to bounce.

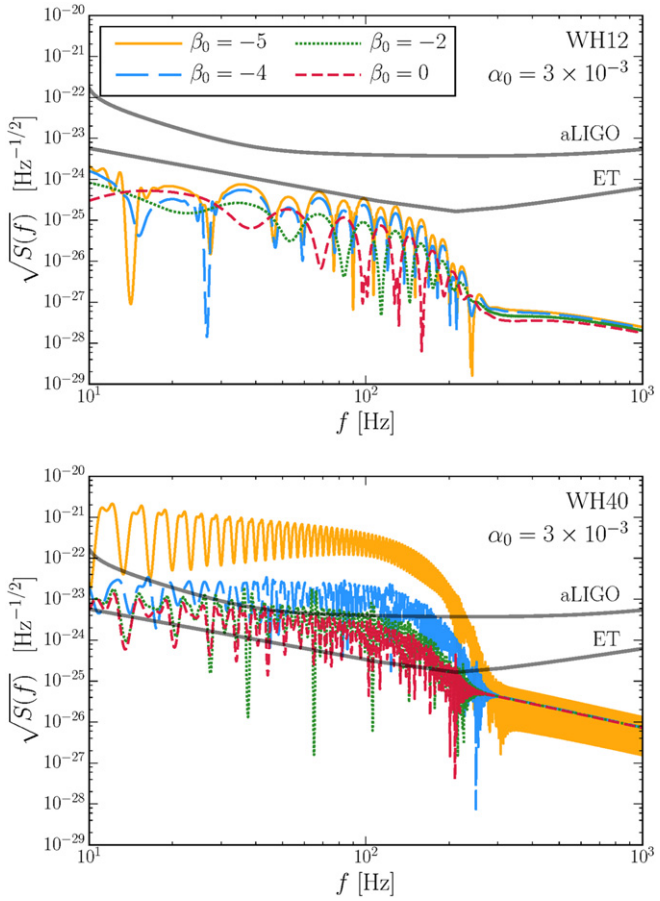

Figure 8. Effect of β_0 on frequency domain waveforms for monopole GWs emitted during stellar collapse. The $M_{\rm ZAMS} = 12M_\odot$ (top) and $40M_\odot$ (bottom) pre-SN models of [100] are evolved using the hybrid EOS with $\Gamma_1 = 1.3$, $\Gamma_2 = 2.5$ and $\Gamma_{\rm th} = 1.35$. Four simulations are presented for fixed $\alpha_0 = 3 \times 10^{-3}$ (marginally allowed by solar-system constraints): $\beta_0 = -5$ (orange, solid), -4 (blue, long-dashed), -2 (green, dotted), 0 (red, short-dashed). These values are compared with current experimental constraints in figure 1. We consider optimally oriented sources placed at $D = 10$ kpc and compare them with the expected sensitivity curves of Advanced LIGO and the Einstein telescope. Waveforms presented in this figure are available at [58].

(iv) Two of the simulations shown in figure 6 (namely $\Gamma_1 = 1.28$, 1.3; $\Gamma_2 = 2.5$; $\Gamma_{\rm th} = 1.35$) for the WH40 profile collapse to BHs. BH formation is triggered when the protoneutron star exceeds its maximum mass and is therefore facilitated and accelerated by smaller values of the adiabatic indices. BH formation generates a very large pulse in the scalar field which dominates the entire GW signal. Spontaneous scalarisation (marginally allowed for the value $\beta_0 = -4.35$ chosen here) before BH formation further enhances the signal. The amplitude of the scalar field signal from this phase is more than an order of magnitude larger than the bounce signal in the absence of BH formation. We expect BH-forming collapse events to be the most promising source of monopole GWs in the context of ST theory.

5.2.2. Effect of the ST parameters. As introduced in section 3.2, PN deviations from GR in ST theories only depend on two parameters, α_0 and β_0. While α_0 mainly controls the perturbative deviation from GR, β_0 is responsible for nonlinear effects such as spontaneous scalarisation. Our primary interest in this section is to explore the effect of these parameters on the detectability of signals with current and future GW detectors and, in particular, comparison with their sensitivity curves.

Figures 7 and 8 show frequency domain waveforms $\sqrt{S_h(f)}$ compared with the expected (design) sensitivity curves $\sqrt{S_n(f)}$ of Advanced LIGO and the Einstein telescope. We use the WH12 and WH40 initial profiles, together with the hybrid EOS with fiducial values $\Gamma_1 = 1.3$, $\Gamma_2 = 2.5$, and $\Gamma_{\rm th} = 1.35$ (see section 3.1). To better disentangle the effect of the two ST parameters, figures 7 and 8 presents a series of simulations where only α_0 (β_0) varies while the other parameter is kept fixed at $\beta_0 = 0$ ($\alpha_0 = 3 \times 10^{-3}$). These two parameter sets overlap at $\alpha_0 = 3 \times 10^{-3}$ and $\beta_0 = 0$ and this specific simulation is shown in both figures. The location of our runs in the (α_0, β_0) parameter space is shown in figure 1. Throughout our analysis, we consider optimally oriented sources placed at a fiducial distance of $D = 10$ kpc, i.e. within the Milky Way.

As mentioned above, the most pronounced feature in the emitted waveform arises from the collapse of the protoneutron star to a BH. As a consequence, the GW strains emitted during collapse of the $M_{\rm ZAMS} = 40M_\odot$ profile WH40 are over an order of magnitude larger than the corresponding signals obtained from the collapse of the WH12 profile. BH formation (possibly enhanced by spontaneous scalarisation—see below) following the protoneutron star phase is the most promising signature of monopole GWs in the context of ST theory.

Simulations presented in figure 7 are performed in ST theory with $\beta_0 = 0$ and various values of α_0, equivalent to Brans–Dicke theory with $\omega_{\rm BD} = (1 - 6\alpha_0^2)/2\alpha_0^2$. Since spontaneously scalarised stars are not permitted in this regime, this set of simulations illustrates the effect of perturbative deviations from GR. In ST theory with $\alpha_0 \sim 3 \times 10^{-3}$, just compatible with the Cassini bound, GW signals generated by BH formation in our Galaxy, are marginally detectable by second-generation ground-based detectors and fall well into the sensitivity range of future experiments like the Einstein telescope. Observation of a BH forming core collapse event with Advanced LIGO therefore has the potential of independently constraining ST theory at a level comparable with the most stringent present tests. Future third-generation observatories, on the other hand, will be able to push the constraint to new levels: $\alpha_0 \lesssim \times 10^{-4}$ corresponding to $|\gamma^{\rm PPN} - 1| \lesssim 2 \times 10^{-8}$; cf equation (3.7). On the other hand, our present results suggest that core collapse forming NSs (such as in our WH12 model) will at best allow for an independent confirmation of existing bounds, even when observed with third-generation observatories.

By analysing the curves in figure 7 quantitatively, we observe that the amplitude of the GW signal scales approximately as α_0^2. One factor of α_0 is evidently due to the local coupling between the scalar field and the detector (see equation (3.23)). In our simulations, however, we find that the amplitude of the emitted scalar field φ also depends (roughly linearly) on α_0. This second factor of α_0 is entirely due to the source dynamics and therefore separate from that arising in the coupling between the wave and the detector at the moment of observation. Even though the dynamics in the matter variables only mildly deviates from the GR case (see figure 5), such perturbative deviations from GR of the order α_0 can leave a significant imprint on the generation of monopole GWs.

The strongest effect of β_0 on the structure of NSs is that of allowing for spontaneously scalarised stars in the range $\beta_0 \lesssim -4.35$. In fact, it is precisely the strength of this effect that enables binary pulsar observations to severely constrain β_0 as displayed in figure 1. For our

simulations using values of β_0 significantly above the spontaneous scalarisation threshold of about -4.35, we only identify a relatively minor variation of the scalar wave with β_0. This is well illustrated by the curves in figure 8 corresponding to $\beta_0 = 0$ and -2. Deviations of this kind can become particularly pronounced for $\beta_0 \lesssim -4.35$ *if* the strongly nonlinear effects of spontaneous scalarisation are triggered [33, 34, 51, 91]; cf figure 8. Whether this effect is triggered in our simulations and, in consequence, the shape and magnitude of the resulting waveform, critically depends on the stellar progenitor.

- If the core collapse leads to a protoneutron star that subsequently collapses to a BH, spontaneous scalarisation can be triggered by the high compactness reached shortly before BH formation, leading to a large enhancement of the GW signal. In the bottom panel of figure 8, we compare the frequency-domain GW signals for the BH-forming WH40 progenitor. Spontaneous scalarisation occurs in a very strong way for the model with $\beta_0 = -5$ (already ruled out by current constraints) and leads to an enhancement of ∼two orders of magnitude in the amplitude compared to models that do not exhibit this strong nonlinear behaviour (cases with $\beta_0 = 0$ and $\beta_0 = -2$). The waveform of the model with $\beta = -4$ (still allowed) is also somewhat enhanced by nonlinear scalar field dynamics. Given the quantitative differences between these waveforms, present and future detectors have the potential of either observing scalar waves from BH-forming core collapse events or use their absence in the data stream to constrain the parameter β_0 beyond current limits. This will, however, require that other uncertain parameters such as the distance to the source etc can be determined with high precision.
- None of our simulations of the progenitor model WH12 leads to BH formation in the time simulated. This is so because this moderate-mass progenitor has a steep density gradient outside its core and thus a lower postbounce accretion rate. If no explosion is launched, a BH would still result, though on a timescale of $\mathcal{O}(10)$ s [26]. Furthermore, we do not observe any signature of spontaneous scalarisation in the waveform or in the protoneutron star of the WH12 model, even for the extreme case $\beta_0 = -5$ (see figure 8, top panel). An analogous conclusion holds for collapse of ST polytropes, see section 3.3. The reason for this absence of spontaneous scalarisation in these models lies in the insufficient compactness of their protoneutron stars. At the end of our simulations, the protoneutron star in model WH12 has a compactness of $m/r \sim 0.05$ (at $r = 10$ km), significantly lower than the threshold of ∼0.2 at which multiple families of stationary solutions appear [89].

The final compactness reached by NS remnants is naturally model dependent and the microphysics implemented in our analysis is greatly simplified by the use of the hybrid EOS. The possibility of triggering spontaneous scalarisation in stellar core collapse forming NSs (as opposed to BHs) clearly requires further exploration with more realistic finite-temperature EOS, which is left to future work. Dissociation of accreting heavy nuclei at the shock and neutrino cooling act indeed in the direction of lowering the effective adiabatic index in the postshock region, thus facilitating a more rapid increase in the protoneutron star's mass and compactness [122]. We probe this expectation within our current framework by evolving the WH12 model with an adiabatic index $\Gamma_{\rm th}$ artificially lowered to 1.25. With such a low value of $\Gamma_{\rm th}$, the shock stalls at a small radius and material accreting through the shock quickly settles onto the protoneutron star, driving up its mass and compactness. At the end of our simulation, at 0.7 s, the protoneutron star in this model has reached a compactness of ∼0.18 and is spontaneously scalarised. Configurations with non-trivial scalar-field profiles are energetically favoured over their weak-field counterparts and the dynamical evolutions naturally settle

there. The GW strain $\sqrt{S_h(f)}$ increases by roughly two orders of magnitude when compared to runs performed using the more realistic value $\Gamma_{\rm th} = 1.35$. Galactic signals from spontaneously scalarised NSs, if formed in core collapse, will likely be detectable by Advanced LIGO even beyond the Cassini bound $\alpha_0 = 3 \times 10^{-3}$. Given its observational potential, this topic definitely merits further investigation with more realistic microphysics.

6. Conclusions

This paper presents an extension of the open-source code GR1D [54] to ST theories of gravity. The required additions to GR1D can be summarised as follows:

(i) generalisation of the flux and source terms in the high-resolution shock capturing scheme according to (2.34)–(2.39) as well as the constraint equations (2.21) and (2.22) for the metric components;
(ii) implementation of the evolution of the scalar field according to equations (2.26)–(2.28) using standard finite differencing;
(iii) outgoing radiation boundary condition for the scalar field (2.31) and (2.32).

The scalar field furthermore introduces a new radiative degree of freedom propagating at the speed of light, which requires a smaller numerical timestep. All presented time evolutions start from one of two types of initial data, (i) polytropic models obtained by solving the time independent limit of the evolution equations and (ii) more realistic pre-SN models from zero-age main-sequence stars of masses 12 and $40M_\odot$ [100].

In this framework, we have simulated a large number of collapse scenarios which are characterised by five parameters: the linear and quadratic coefficients α_0 and β_0 determining the coupling function of the ST theory and the adiabatic indices Γ_1, Γ_2 and $\Gamma_{\rm th}$, characterising the phenomenological hybrid EOS used in the time evolution. We summarise our main observations as follows.

- The most prominent GW signals are detected from the collapse of progenitor stars that form BHs after a protoneutron star phase (such as the $M_{\rm ZAMS} = 40M_\odot$ model of [100]), as opposed to collapse events forming long-term stable NSs. The collapse of protoneutron stars to BHs is the most promising dynamical feature for monopole gravitational radiation in the context of ST theories.
- The dynamical features in the matter fields (density, mass function, pressure) resemble closely those obtained in the general relativistic limit $\alpha_0 = \beta_0 = 0$. In other words, the effect of the scalar field on the matter dynamics is weak.
- The opposite is not true. The scalar radiation or GW *breathing mode* is sensitive to the specifics of the collapse dynamics as well as the choice of ST parameters α_0 and β_0. The observed dependencies are of the kind one would intuitively expect. EOS and progenitors giving rise to more compact post-collapse configurations result in stronger radiation and the amplitude of the scalar wave sensitively increases with α_0 with approximately a quadratic dependence.
- The ST parameter β_0 is known to generate strongly nonlinear effects in the scalar field for $\beta_0 \lesssim -4.35$, the so-called *spontaneous scalarisation* [33, 34]. For progenitors collapsing to BHs after a protoneutron star phase, transition of the central core to a spontaneously scalarised configuration before BH formation further enhances the outgoing GW signal. For progenitors forming NSs but not BHs, we do not find spontaneously scalarised

configurations for physically plausible values of the adiabatic indices in our hybrid EOS. We attribute this to the stellar compactness achieved in those collapse scenarios being insufficient to trigger spontaneous scalarisation. This observation may be an artefact of our simplistic treatment of microphysics in our simulations.

- We have extracted waveforms from a large set of simulations and compared their amplitude for the case of a fiducial distance $D = 10$ kpc with the sensitivity curves of Advanced LIGO and the Einstein telescope. Given the present constraints from the Cassini probe, $\alpha_0 \lesssim 3 \times 10^{-3}$, scalar radiation may be marginally detectable from galactic sources. This offers the possibility of providing constraints on ST theory with GW observations in case of a favourable event occurring in the Milky Way. Considerable power is emitted at low frequencies $f \lesssim 10$ Hz, thus making core collapse in ST theory ideal sources for future experiments such as DECIGO [112].

The impact of more realistic microphysics, as for example nuclear dissociation at the shock and neutrino cooling, on the compactness of the core and, thus, its degree of scalarisation, represents one key extension left for future work. Our analysis has shown that the massive increase in wave amplitudes due to spontaneous scalarisation and BH formation has the potential to drastically increase the range for detection. The $\mathcal{O}(10^3)$ waveforms generated for this work were completed in less than a week using $\mathcal{O}(10^2)$ CPU cores simultaneously. A moderate increase in the computational resources will make simulations using tabulated finite-temperature EOS feasible. Since the matter fields' dynamics is very similar to the GR case, one may perhaps take advantage of existing GR simulations and simulate the scalar field evolution using such GR results as backgrounds. A further numerical improvement may consist in computing (perhaps iteratively) approximate initial conditions for the scalar field from existing pre-collapse stellar models (such as WH12 and WH40 used in this paper), in order to reduce the brief unphysical transient in the GW signal.

Aside from the treatment of the microphysics, our study offers further scope for extension. The effects of multiple scalar fields in ST theories on gravitational collapse remains largely unknown in spite of some early studies [13] (see [43] for an analysis of static NS solutions in this framework), but represents a relatively minor addition to our code. The same holds for ST theories with non-vanishing potential, as for example massive fields [99, 123].

As GW physics and astronomy are ushering in a new era, the community will be offered a wealth of unprecedented opportunities to observationally test generalisations of GR. Stellar collapse clearly offers a vast potential for such fundamental tests.

Acknowledgments

We thank Chris Moore, Jerome Novak, Evan O'Connor, Norbert Wex, Paulo Freire and Carlos Sopuerta for fruitful discussions. DG is supported by the UK STFC and the Isaac Newton Studentship of the University of Cambridge. US is supported by the H2020 ERC Consolidator Grant 'Matter and strong-field gravity: New frontiers in Einstein's theory' grant agreement No. MaGRaTh-646597, the European Union's Horizon 2020 research and innovation programme under the Marie Skludowska-Curie grant agreement 690904, the STFC Consolidator Grant No. ST/L000636/1, the SDSC Comet and TACC Stampede clusters through NSF-XSEDE Award Nos. TG-PHY090003 and TG-PHY100033, the Cambridge High Performance Computing Service Supercomputer Darwin using Strategic Research Infrastructure Funding from the HEFCE and the STFC, and DiRAC's Cosmos Shared Memory system through BIS Grant No. ST/J005673/1 and STFC Grant Nos. ST/H008586/1, ST/K00333X/1. CDO is partially supported by NSF under award Nos. CAREER PHY-

1151197, and PHY-1404569, and by the International Research Unit of Advanced Future Studies, Kyoto University. Figures were generated using the PYTHON-based MATPLOTLIB package [124]. This article has been assigned Yukawa Institute report number YITP-16-14.

References

[1] Berti E *et al* 2015 *Class. Quantum Grav.* **32** 243001
[2] The LIGO Scientific Collaboration and The Virgo Collaboration 2016 arXiv:1602.03841
[3] Will C M 2014 *Living Rev. Relativ.* **17** 4
[4] Psaltis D 2008 *Living Rev. Relativ.* **11** 9
[5] Bertone G, Hooper D and Silk J 2005 *Phys. Rep.* **405** 279–390
[6] Copeland E J, Sami M and Tsujikawa S 2006 *Int. J. Mod. Phys.* D **15** 1753–935
[7] Spergel D N 2015 *Science* **347** 1100–2
[8] Burgess C P 2004 *Living Rev. Relativ.* **7** 5
[9] Hawking S W and Penrose R 1970 *Proc. R. Soc.* A **314** 529–48
[10] Jordan P 1959 *Z. Phys.* **157** 112–21
[11] Fierz M 1956 *Helv. Phys. Acta* **29** 128–34
[12] Brans C and Dicke R H 1961 *Phys. Rev.* **124** 925–35
[13] Damour T and Esposito-Farese G 1992 *Class. Quantum Grav.* **9** 2093–176
[14] Chiba T, Harada T and Nakao K 1997 *Prog. Theor. Phys. Suppl.* **128** 335–72
[15] Fujii Y and Maeda K I 2003 *The Scalar-Tensor Theory of Gravitation* (Cambridge: Cambridge University Press)
[16] Sotiriou T P 2014 *Gravity and Scalar Fields* (*Lecture Notes in Physics* vol 892) ed E Papantonopoulos (Berlin: Springer) pp 3–24
[17] Faraoni V 2004 *Cosmology in Scalar-Tensor Gravity* (Dordrecht: Springer)
[18] Hawking S W 1972 *Commun. Math. Phys.* **25** 167–71
[19] Thorne K S and Dykla J J 1971 *Astrophys. J.* **166** L35
[20] Chase J E 1970 *Commun. Math. Phys.* **19** 276–88
[21] Bekenstein J D 1997 Black hole hair: twenty-five years after *2nd Int. A.D. Sahkarov Conf. on Physics* ed A J Dremin and A M Semikhatov p 216 (arXiv:gr-qc/9605059)
[22] Herdeiro C A R and Radu E 2015 *Int. J. Mod. Phys.* D **24** 1542014
[23] Will C M and Zaglauer H W 1989 *Astrophys. J.* **346** 366–77
[24] Healy J, Bode T, Haas R, Pazos E, Laguna P, Shoemaker D M and Yunes N 2012 *Class. Quantum Grav.* **29** 232002
[25] Berti E, Cardoso V, Gualtieri L, Horbatsch M and Sperhake U 2013 *Phys. Rev.* D **87** 124020
[26] O'Connor E and Ott C D 2011 *Astrophys. J.* **730** 70
[27] Clausen D, Piro A L and Ott C D 2015 *Astrophys. J.* **799** 190
[28] Sukhbold T, Ertl T, Woosley S E, Brown J M and Janka H T 2016 *Astrophys. J.* **821** 38
[29] Bethe H A 1990 *Rev. Mod. Phys.* **62** 801–66
[30] Janka H T, Langanke K, Marek A, Martínez-Pinedo G and Müller B 2007 *Phys. Rep.* **442** 38–74
[31] Burrows A, Dessart L, Livne E, Ott C D and Murphy J 2007 *Astrophys. J.* **664** 416–34
[32] Ugliano M, Janka H T, Marek A and Arcones A 2012 *Astrophys. J.* **757** 69
[33] Damour T and Esposito-Farese G 1993 *Phys. Rev. Lett.* **70** 2220–3
[34] Damour T and Esposito-Farèse G 1996 *Phys. Rev.* D **54** 1474–91
[35] Barausse E, Palenzuela C, Ponce M and Lehner L 2013 *Phys. Rev.* D **87** 081506
[36] Palenzuela C, Barausse E, Ponce M and Lehner L 2014 *Phys. Rev.* D **89** 044024
[37] Shibata M, Taniguchi K, Okawa H and Buonanno A 2014 *Phys. Rev.* D **89** 084005
[38] Abbott B P *et al* 2016 *Phys. Rev. Lett.* **116** 061102
[39] Ott C D 2009 *Class. Quantum Grav.* **26** 063001
[40] Doneva D D, Yazadjiev S S, Stergioulas N and Kokkotas K D 2013 *Phys. Rev.* D **88** 084060
[41] Mendes R F P 2015 *Phys. Rev.* D **91** 064024
[42] Silva H O, Macedo C F B, Berti E and Crispino L C B 2015 *Class. Quantum Grav.* **32** 145008
[43] Horbatsch M, Silva H O, Gerosa D, Pani P, Berti E, Gualtieri L and Sperhake U 2015 *Class. Quantum Grav.* **32** 204001
[44] Palenzuela C and Liebling S 2016 *Phys. Rev.* D **93** 044009
[45] Matsuda T and Nariai H 1973 *Prog. Theor. Phys.* **49** 1195–204
[46] Scheel M A, Shapiro S L and Teukolsky S A 1995 *Phys. Rev.* D **51** 4208–35

[47] Scheel M A, Shapiro S L and Teukolsky S A 1995 *Phys. Rev.* D **51** 4236–49
[48] Shibata M, Nakao K and Nakamura T 1994 *Phys. Rev.* D **50** 7304–17
[49] Harada T, Chiba T, Nakao K I and Nakamura T 1997 *Phys. Rev.* D **55** 2024–37
[50] Novak J 1998 *Phys. Rev.* D **57** 4789–801
[51] Novak J 1998 *Phys. Rev.* D **58** 064019
[52] Novak J and Ibáñez J M 2000 *Astrophys. J.* **533** 392–405
[53] Dimmelmeier H 1998 Numerical calculations of hydrodynamic gravitational collapse and its observational consequences in scalar-tensor theories of gravity *Diploma Thesis* University of Regensburg (http://hdl.handle.net/11858/00-001M-0000-0013-59C8-2)
[54] O'Connor E and Ott C D 2010 *Class. Quantum Grav.* **27** 114103
[55] The LIGO Scientific Collaboration 2015 *Class. Quantum Grav.* **32** 074001
[56] The LIGO Scientific Collaboration and The Virgo Collaboration 2016 *Phys. Rev. Lett.* **116** 131103
[57] Punturo M *et al* 2010 *Class. Quantum Grav.* **27** 194002
[58] www.damtp.cam.ac.uk/user/dg438/corecollapse
www.davidegerosa.com/corecollapse
www.stellarcollapse.org/gerosaetal2016
[59] Salgado M 2006 *Class. Quantum Grav.* **23** 4719–41
[60] Damour T 2007 *Proc. 6th SIGRAV Graduate School in Contemporary Relativity and Gravitational Physics: a Century from Einstein Relativity: Probing Gravity Theories in Binary Systems (Como, Italy, 17–21 May 2005)* (Berlin: Springer)
[61] Bertotti B, Iess L and Tortora P 2003 *Nature* **425** 374–6
[62] Salgado M, Martínez del Río D, Alcubierre M and Núñez D 2008 *Phys. Rev.* D **77** 104010
[63] Romero J V, Miralles J M, Ibáñez J A and Pons J A 1997 General relativistic collapse of hot stellar cores *Some Topics on General Relativity and Gravitational Radiation* ed J A Miralles *et al* (Biarritz: Atlantica Séguier) p 289
[64] Font J A, Miller M, Suen W M and Tobias M 2000 *Phys. Rev.* D **61** 044011
[65] Font J A 2008 *Living Rev. Relativ.* **11** 7
[66] Birkhoff G D and Langer R E 1923 *Relativity and Modern Physics* (Cambridge, MA: Harvard University Press)
[67] Krori K D and Nandy D 1977 *J. Phys. A: Math. Gen.* **10** 993–6
[68] Sommerfeld A 1949 *Partial Differential Equation in Physics* (New York: Academic)
[69] LeVeque R J 1992 *Numerical Methods for Conservation Laws* 2nd edn (Basel: Birkhäuser)
[70] Baumgarte T W and Shapiro S L 2010 *Numerical Relativity: Solving Einstein's Equations on the Computer* (Cambridge: Cambridge University Press)
[71] Janka H T, Zwerger T and Moenchmeyer R 1993 *Astron. Astrophys.* **268** 360–8
[72] Zwerger T and Mueller E 1997 *Astron. Astrophys.* **320** 209–27
[73] Dimmelmeier H, Font J A and Müller E 2002 *Astron. Astrophys.* **393** 523–42
[74] Dimmelmeier H, Ott C D, Janka H T, Marek A and Müller E 2007 *Phys. Rev. Lett.* **98** 251101
[75] Dimmelmeier H, Ott C D, Marek A and Janka H T 2008 *Phys. Rev.* D **78** 064056
[76] Shapiro S L and Teukolsky S A 1983 *Black Holes, White Dwarfs and Neutron Stars: The Physics of Compact Objects* (New York: Wiley)
[77] Lattimer J M and Douglas S F 1991 *Nucl. Phys.* A **535** 331–76
[78] Lattimer J M, Pethick C J, Ravenhall D G and Lamb D Q 1985 *Nucl. Phys.* A **432** 646–742
[79] Shen H, Toki H, Oyamatsu K and Sumiyoshi K 1998 *Nucl. Phys.* A **637** 435–50
[80] Shen H, Toki H, Oyamatsu K and Sumiyoshi K 1998 *Prog. Theor. Phys.* **100** 1013–31
[81] Shen H, Toki H, Oyamatsu K and Sumiyoshi K 2011 *Astrophys. J. Suppl. Ser.* **197** 20
[82] Eddington A S 1923 *The Mathematical Theory of Relativity* (Cambridge: Cambridge University Press)
[83] Will C M 1993 *Theory and Experiment in Gravitational Physics* (Cambridge: Cambridge University Press)
[84] Damour T and Esposito-Farèse G 1996 *Phys. Rev.* D **53** 5541–78
[85] Damour T and Nordtvedt K 1993 *Phys. Rev.* D **48** 3436–50
[86] Damour T and Nordtvedt K 1993 *Phys. Rev. Lett.* **70** 2217–9
[87] Järv L, Kuusk P and Saal M 2008 *Phys. Rev.* D **78** 083530
[88] Sampson L, Yunes N, Cornish N, Ponce M, Barausse E, Klein A, Palenzuela C and Lehner L 2014 *Phys. Rev.* D **90** 124091

[89] Esposito-Farèse G 2004 Tests of scalar-tensor gravity, phi in the sky *The Quest for Cosmological Scalar Fields* (*American Institute of Physics Conference Series* vol 736) ed C J A P Martins *et al* pp 35–52 (arXiv:gr-qc/0409081)
[90] Horbatsch M W and Burgess C P 2011 *J. Cosmol. Astropart. Phys.* **8** 027
[91] Harada T 1998 *Phys. Rev.* D **57** 4802–11
[92] Harada T 1997 *Prog. Theor. Phys.* **98** 359–79
[93] Shapiro I I 1990 Solar system tests of general relativity: recent results and present plans *General Relativity Gravitation, 1989* ed N Ashby *et al* (Cambridge: Cambridge University Press) p 313
[94] Williams J G, Turyshev S G and Boggs D H 2009 *Int. J. Mod. Phys.* D **18** 1129–75
[95] Shapiro S S, Davis J L, Lebach D E and Gregory J S 2004 *Phys. Rev. Lett.* **92** 121101
[96] Wex N 2014 arXiv:1402.5594
[97] Freire P C C, Wex N, Esposito-Farèse G, Verbiest J P W, Bailes M, Jacoby B A, Kramer M, Stairs I H, Antoniadis J and Janssen G H 2012 *Mon. Not. R. Astron. Soc.* **423** 3328–43
[98] Antoniadis J *et al* 2013 *Science* **340** 448
[99] Ramazanoğlu F M and Pretorius F 2016 *Phys. Rev.* D **93** 064005
[100] Woosley S E and Heger A 2007 *Phys. Rep.* **442** 269–83
[101] Tolman R C 1939 *Phys. Rev.* **55** 364–73
[102] Oppenheimer J R and Volkoff G M 1939 *Phys. Rev.* **55** 374–81
[103] Press W H, Flannery B P, Teukolsky S A and Vetterling W T 1989 *Numerical Recipes in C. The Art of Scientific Computing* (Cambridge: Cambridge University Press)
[104] Weaver T A, Zimmerman G B and Woosley S E 1978 *Astrophys. J.* **225** 1021–9
[105] Woosley S E, Heger A and Weaver T A 2002 *Rev. Mod. Phys.* **74** 1015–71
[106] Misner C W, Thorne K S and Wheeler J A 1973 *Gravitation* (San Francisco, CA: Freeman)
[107] Nishizawa A, Taruya A, Hayama K, Kawamura S and Sakagami M A 2009 *Phys. Rev.* D **79** 082002
[108] Yunes N and Siemens X 2013 *Living Rev. Relativ.* **16** 9
[109] Moore C J, Cole R H and Berry C P L 2015 *Class. Quantum Grav.* **32** 015014
[110] Sathyaprakash B S and Schutz B F 2009 *Living Rev. Relativ.* **12** 2
[111] The LIGO Scientific Collaboration 2009 https://dcc.ligo.org/cgi-bin/DocDB/ShowDocument?docid = m060056
[112] Kawamura S *et al* 2011 *Class. Quantum Grav.* **28** 094011
[113] Barausse E, Cardoso V and Pani P 2014 *Phys. Rev.* D **89** 104059
[114] Ivezić Ż, Connolly A, VanderPlas J and Gray A 2013 *Statistics, Data Mining, and Machine Learning in Astronomy* (Princeton, NJ: Princeton University Press)
[115] O'Connor E and Ott C D 2013 *Astrophys. J.* **762** 126
[116] www.stellarcollapse.org/GR1Dv2
[117] O'Connor E 2015 *Astrophys. J. Suppl. Ser.* **219** 24
[118] Gustafsson B, Kreiss H O and Oliger J 1995 *Time-Dependent Problems and Difference Methods* 2nd edn (New York: Wiley)
[119] Alcubierre M 2008 *Introduction to 3 + 1 Numerical Relativity* (Oxford: Oxford University Press)
[120] Kreiss H O and Oliger J 1973 *Methods for the Approximate Solution of Time Dependent problems* (Geneva: World Meteorological Organization, International Council of Scientific Unions)
[121] Chruściel P T, Costa J L and Heusler M 2012 *Living Rev. Relativ.* **15** 7
[122] Radice D, Ott C D, Abdikamalov E, Couch S M, Haas R and Schnetter E 2016 *Astrophys. J.* **820** 76
[123] Alsing J, Berti E, Will C M and Zaglauer H 2012 *Phys. Rev.* D **85** 064041
[124] Hunter J D 2007 *Comput. Sci. Eng.* **9** 90–5